Lines and Boxes: Unmasking Dynamical Dark Matter through Correlations in the MeV Gamma-Ray Spectrum

Kimberly K. Boddy[1*], Keith R. Dienes[2,3†], Doojin Kim[4‡], Jason Kumar[1§], Jong-Chul Park[5¶], Brooks Thomas[6,7**]

[1] *Department of Physics & Astronomy, University of Hawaii, Honolulu, HI 96822 USA*
[2] *Department of Physics, University of Arizona, Tucson, AZ 85721 USA*
[3] *Department of Physics, University of Maryland, College Park, MD 20742 USA*
[4] *Department of Physics, University of Florida, Gainesville, FL 32611 USA*
[5] *Department of Physics, Chungnam National University, Daejeon 34134 Korea*
[6] *Department of Physics, Colorado College, Colorado Springs, CO 80903 USA*
[7] *Department of Physics, Lafayette College, Easton, PA 18042 USA*

arXiv:1606.07440v2 [hep-ph] 9 Apr 2017

Identifying signatures of dark matter at indirect-detection experiments is generally more challenging for scenarios involving non-minimal dark sectors such as Dynamical Dark Matter (DDM) than for scenarios involving a single dark particle. This additional difficulty arises because the partitioning of the total dark-matter abundance across an ensemble of different constituent particles with different masses tends to "smear" the injection spectra of photons and other cosmic-ray particles that are produced via dark-matter annihilation or decay. As a result, the imprints of the dark sector on these cosmic-ray flux spectra typically take the form of continuum features rather than sharp peaks or lines. In this paper, however, we identify an unambiguous signature of non-minimal dark sectors such as DDM which can overcome these issues and potentially be observed at gamma-ray telescopes operating in the MeV range. We discuss the specific situations in which this signature can arise, and demonstrate that this signature can be exploited in order to significantly enhance our ability to resolve the unique spectral features of DDM and other non-minimal dark sectors at future gamma-ray facilities.

I. INTRODUCTION

Understanding the properties of the dark sector represents one of the great experimental and theoretical challenges facing physics today. Indeed, we even lack insight into such fundamental questions as whether the dark sector is minimal (*e.g.*, consisting of only one or a few dark particle species) or non-minimal (*e.g.*, consisting of many particle species). A pressing phenomenological question, therefore, is to determine how — and to what degree it is even possible — to experimentally distinguish non-minimal dark sectors from their more traditional, minimal counterparts. This is especially true for scenarios within the Dynamical Dark Matter (DDM) [1, 2] framework — a framework for dark-matter physics in which the dark-matter "candidate" is an ensemble consisting of a potentially vast number of individual constituent particle species exhibiting a variety of masses, decay widths, and cosmological abundances. Such DDM dark sectors give rise to collective phenomena that transcend expectations based on traditional dark-matter frameworks. For example, the phenomenological viability of such a DDM ensemble as a representation of the dark sector rests not on the stability of each of these species individually, but rather on a subtle balancing between decay widths and cosmological abundances across the ensemble as a whole.

In many DDM scenarios, the ensemble constituents share the same or similar quantum numbers. In such cases, the detection channels through which one might hope to find evidence of such an ensemble are essentially identical to those in which one would seek evidence of a traditional dark-matter candidate with the identical quantum numbers. However, even if the ensemble constituents share similar quantum numbers, they generically differ in their masses and couplings. As a result, it is often possible to distinguish DDM ensembles and other non-minimal dark sectors experimentally by analyzing the distributions of relevant kinematic variables. At direct-detection experiments, for example, the relevant distribution is the recoil-energy spectrum of the recoiling nucleus [3]. Likewise, at indirect-detection experiments, the relevant kinematic distributions are the differential flux spectra of the SM particles which can be produced via dark-matter annihilation or decay [4]. Finally, at colliders, the relevant distributions are those corresponding to a number of well-chosen kinematic variables formed from the momenta of Standard-Model (SM) particles produced alongside the dark-matter particles. The information contained in the full shapes of these distributions can be used to distinguish DDM from traditional dark-matter scenarios [5, 6], and indeed can be used to

*E-mail address: kboddy@hawaii.edu
†E-mail address: dienes@email.arizona.edu
‡E-mail address: immworry@ufl.edu
§E-mail address: jkumar@hawaii.edu
¶E-mail address: jcpark@cnu.ac.kr
**E-mail address: thomasbd@lafayette.edu

distinguish a variety of other non-minimal dark-matter scenarios as well [7–10].

A variety of cosmic-ray particles — among them electrons, positrons, photons, antiprotons, neutrinos, and antideuterons — can potentially yield information about the nature of the dark matter. For example, it has been shown that DDM ensembles can give rise to characteristic signatures [4] in the flux spectra of electrons and positrons which can account for the positron excess observed by PAMELA [11], AMS-02 [12], and a host of other experiments — most notably without predicting an abrupt downturn in the positron fraction at high energies. However, of all cosmic-ray particles whose flux spectra we have the ability to measure, photons are the particles that afford the greatest potential for probing the structure of the dark sector. This is true primarily for two reasons. First, the spectrum of photons injected by a particular source is deformed far less by interactions with the interstellar medium (ISM) than are the spectra associated with most other cosmic-ray particles. Thus, features imprinted on the photon spectrum at injection — features which might be indicative of dark-sector non-minimality — are not washed out as a result of their propagation through this medium. Second, unlike neutrinos (which are also largely unaffected by propagation through the ISM), photons are easy to detect and their energies and directions can be measured with great precision.

It nevertheless remains true that identifying such signatures at indirect-detection experiments is generally more challenging for DDM scenarios than for other, more traditional dark-matter scenarios. This is because the injection spectra of photons and other cosmic-ray particles from dark-matter annihilation or decay within DDM scenarios are subject to an additional "smearing" effect due to the partitioning of the total dark-matter abundance across an ensemble of constituent particles with a range of masses. Thus, the characteristic imprints which these ensembles leave in the corresponding flux spectra typically take the form of continuum features rather than sharp peaks or lines. This is especially true for cases in which the splittings between the masses of ensemble constituents are small. Disentangling continuum features from astrophysical backgrounds is generally significantly more challenging than disentangling sharp peaks or lines. Moreover, even in situations in which such features can be robustly identified, it is often impossible to conclusively determine whether dark matter or some more mundane astrophysical process is responsible.

In this paper, we identify an unambiguous signature of DDM (and of non-minimal dark sectors more generally) which can serve to overcome these issues and potentially be observed at gamma-ray telescopes sensitive to photons with energies in the $\mathcal{O}(1-100)$ MeV range. This signature arises in cases in which each of the ensemble constituents annihilates or decays predominately into a primary photon and a neutral pion [13], the latter subsequently decaying into a pair of secondary photons.

In general, the primary photons give rise to a line-like feature, while the secondary photons give rise to a characteristic box-like feature whose width is related to the energy (or boost) of the decaying pion. (We review the kinematics of these processes in the Appendix.) In the case of a single dark-matter species, this combination of a line-like feature and a box-like feature is notable and distinctive. Such features have previously been studied, *e.g.*, in Refs. [13–15]. In the case of a DDM ensemble, by contrast, the primary photons give rise to a *set* of line-like features while the secondary photons give rise to a *set* of box-like features. In this paper, we are particularly interested in the regime in which the splitting between constituent masses is small compared to the energy resolution of the telescope. In such cases, the set of line-like features will appear a single effective *continuum* spectral feature. Likewise, the pion energies will also form an effective continuum which then produces a continuum of box-like features. Note that in this context the pion energies will form an effective continuum because these pions are produced via the direct annihilation or decay of the different DDM ensemble components which themselves exhibit an effective continuum of masses. This is therefore somewhat different than the continuous pion spectra that might emerge through multiple sequential decays, as in Refs. [16, 17], or via n-body decays with $n \geq 3$.

Taken in isolation, each of these two spectral features reveals information about the properties of the DDM ensemble. However, what makes this signature particularly advantageous from the perspective of distinguishing between minimal and non-minimal DDM dark sectors is that the spectral shapes of these two features are *correlated*. Thus, a comparison between the information independently extracted from these two continuum features can provide a powerful consistency check that they indeed have a common underlying origin in terms of a DDM ensemble. Indeed, it was shown in Ref. [13] that for a single-particle dark-matter candidate which decays into this same final state, correlations between the properties of the line and box features in the gamma-ray spectrum could be used to reconstruct the mass of the dark-matter particle. By contrast, in a DDM context, we shall see that the correlations between the corresponding continuum features can be used to reconstruct the fundamental relations which describe how the the masses, abundances, and lifetimes of the ensemble constituents scale across the ensemble as a whole.

This paper is organized as follows. In Sect. II, we discuss the circumstances under which the constituents of a DDM ensemble annihilate or decay predominately to a $\gamma\pi^0$ final state. We also establish the conventions we shall use for parametrizing such an ensemble. In Sect. III, we then calculate the contribution to the differential photon flux which arises from dark-matter annihilation or decay in such scenarios. We also discuss the two distinctive features which arise in the flux spectrum and examine how the spectral shapes of these features, and the degree to which they overlap, vary as a function of the pa-

rameters which characterize the ensemble. In Sect. IV, we investigate the prospects of identifying these spectral features in the diffuse galactic gamma-ray spectrum and in the gamma-ray spectra of dwarf spheroidal galaxies at the next generation of gamma-ray telescopes, and in Sect. V we examine the degree to which the underlying parameters which characterize the DDM ensemble can be extracted from the spectral shapes of these features. Finally, in Sect. VI, we summarize our conclusions and provide an outlook for future work, while in the Appendix we review the kinematics leading to line-like and box-like features in the photon spectrum.

II. DDM ENSEMBLES AND THEIR DECAYS TO PHOTONS AND PIONS

Within the context of DDM framework [1, 2], the dark sector comprises a potentially vast ensemble of individual particle species ϕ_n whose cosmological abundances Ω_n are balanced against their decay widths Γ_n in such a way as to ensure consistency with observational data. It turns out that DDM ensembles arise naturally in a variety of well-motivated extensions of the SM; these include scenarios which involve extra spacetime dimensions [1, 2, 18], large spontaneously-broken symmetry groups [19], confining hidden-sector gauge groups [20], or bulk physics in open string theories [20, 21]. In what follows, we adopt the convention that the index $n = 0, 1, 2, \ldots, N$ labels the particles in order of increasing mass.

Our principal aim in this paper is to study the astrophysical gamma-ray signatures associated with DDM ensembles in which the ensemble constituents annihilate or decay predominately into a $\gamma\pi^0$ final state (with a subsequent pion decay $\pi^0 \to \gamma\gamma$), and to determine the degree to which information about the ensemble can be extracted from these signatures. Such final states can arise in DDM scenarios in which the ϕ_n couple directly to quarks via an effective contact operator [13]. The structure of this operator can be inferred from the fact that the final state $\gamma\pi^0$ is odd under charge-conjugation. Under the assumption that the $SU(2)$ weak interaction can be neglected and that the fundamental interactions between the ensemble constituents and the SM fields are C-invariant, the initial state must therefore be C-odd as well. One possible operator structure which possesses the appropriate symmetry properties is

$$\mathcal{O}_n \;=\; c_n \, B_n^\mu \, \bar{q} \gamma_\mu q \tag{2.1}$$

where c_n is an operator coefficient and where B_n^μ is a C-odd quantity involving the ϕ_n fields alone. One situation in which an operator of this sort arises is that in which the ϕ_n are spin-1 fields ϕ_n^μ and corresponds to the case in which B_n^μ is identified with the field ϕ_n^μ itself. In this case, the operator gives rise to decay processes of the form $\phi_n \to \gamma\pi^0$. Another situation in which such an operator arises is that in which $B_n^\mu = \mathcal{J}_n^\mu/\Lambda^2$, where $\mathcal{J}_n^\mu$ is an approximately conserved current associated with the particle number of the ensemble constituent ϕ_n. In this case, the operator gives rise to annihilation processes of the form $\phi_n^\dagger \phi_n \to \gamma\pi^0$. In both of these cases, the fundamental interaction between the dark ensemble constituents ϕ_n and SM quarks gives rise to an effective operator of the form [13]

$$\mathcal{O}_{n,\text{eff}} \;=\; \frac{e\, c_n}{16\pi^2 f_\pi} B_{\mu,n} \, F_{\nu\rho} \, (\partial_\sigma \pi^0) \, \epsilon^{\mu\nu\rho\sigma} \tag{2.2}$$

in the low-energy confined phase of the theory.

We have shown that there exists a self-consistent mechanism through which the constituents of a DDM ensemble can be coupled to the photon and neutral-pion fields. However, whether or not processes resulting in a $\gamma\pi^0$ final state dominate the decay width or annihilation cross-section of a given ϕ_n also depends on the center-of-mass (CM) energy $\sqrt{s_n}$ associated with those processes. Since a number of considerations imply that the velocities of dark-matter particles within the halos of galaxies are non-relativistic, the CM energy for the annihilation or decay of an ensemble constituent with mass m_n is well approximated by

$$\sqrt{s_n} \;\approx\; \begin{cases} 2m_n & \text{for annihilation} \\ m_n & \text{for decay} \, . \end{cases} \tag{2.3}$$

Moreover, the assumption that the dark matter is non-relativistic also implies that the CM frame for annihilating/decaying dark-matter particles is effectively equivalent to the rest frame of the instrument which detects the annihilation/decay products.

In the regime in which $\sqrt{s_n} < m_{\pi^0}$, annihilation/decay to a photon and an on-shell π^0 is kinematically forbidden. Annihilation/decay to a three-photon final state can still proceed in this regime via an off-shell π^0, but processes of this sort do not give rise to the same characteristic features in the photon spectrum. On the other hand, in the regime in which $\sqrt{s_n} > 2m_{\pi^\pm}$, the annihilation/decay of ϕ_n to $\pi^+\pi^-$ is kinematically allowed, but the photons produced as final-state radiation in conjunction with charged-pion production can contribute significantly to the photon flux and overwhelm the contribution from $\gamma\pi^0$. Thus, the range of CM energies for which the $\gamma\pi^0$ channel provides the dominant contribution to the photon flux is given by

$$m_{\pi^0} < \sqrt{s_n} < 2m_{\pi^\pm} \; , \tag{2.4}$$

corresponding to the dark-matter mass ranges

$$\begin{cases} \frac{1}{2} m_{\pi^0} < m_n < m_{\pi^\pm} & \text{for annihilation} \\ m_{\pi^0} < m_n < 2m_{\pi^\pm} & \text{for decay} \, . \end{cases} \tag{2.5}$$

For simplicity, in what follows we shall focus on DDM ensembles in which the masses of all of the ensemble constituents lie within this range. We are therefore interested in DDM ensembles in which the mass scale of

the ϕ_n is of order $m_n \sim \mathcal{O}(100)$ MeV. Indeed, the collective contribution to the photon flux from the annihilation/decay of any lighter constituents in the DDM ensemble is typically negligible unless the density of such states is enormous.

For an ensemble constituent within our chosen mass range, the $\gamma\pi^0$ channel generically yields the dominant contribution to the photon flux. The only other two-body final states which are consistent with the symmetries of the theory and kinematically accessible within the range in Eq. (2.4) are $\bar{\nu}\nu$, e^+e^-, and $\mu^+\mu^-$. The first of these is irrelevant for photoproduction, while the contribution to the photon flux from the other two are necessarily suppressed by additional factors of either α or $s_n G_F$, where G_F is the Fermi constant. Consequently these processes will be comparatively insignificant whenever the $\gamma\pi^0$ state is accessible. The contributions associated with final states involving three or more SM particles are likewise suppressed.

In general, the underlying mass spectrum of our DDM ensemble depends on the type of ensemble under study, and as such it can be arbitrary. For concreteness, however, we shall focus on the case in which the mass spectrum of our DDM ensemble takes the generic form

$$m_n \;=\; m_0 + n^\delta \Delta m \tag{2.6}$$

where m_0 is the mass of ϕ_0 (the lightest of the ϕ_n) and where the mass splitting Δm and scaling exponent δ are free parameters describing our underlying DDM ensemble. Indeed, many realistic DDM ensembles have mass spectra which follow exactly this generic form. Thus, the spectrum of corresponding CM energies takes the form

$$\sqrt{s_n} \;=\; \sqrt{s_0} + n^\delta \Delta(\sqrt{s}) \tag{2.7}$$

where $\Delta(\sqrt{s}) = \Delta m$ for decay and $\Delta(\sqrt{s}) = 2\Delta m$ for annihilation. The splittings $\Delta(\sqrt{s_n}) \equiv \sqrt{s_{n+1}} - \sqrt{s_n}$ between the CM energies for the annihilation/decay of adjacent ensemble states are therefore given by

$$\Delta(\sqrt{s_n}) = \left[(n+1)^\delta - n^\delta\right] \Delta(\sqrt{s}) \;. \tag{2.8}$$

The case with $\delta = 1$ is particularly interesting, occurring when ϕ_n are the modes in a Kaluza-Klein tower. We shall therefore focus on this case in what follows. For this value of δ, the mass splitting $m_{n+1} - m_n$ is uniform across the ensemble, and $\Delta(\sqrt{s_n}) \equiv \Delta(\sqrt{s})$ for all n.

III. GAMMA-RAY SPECTRUM FROM DDM ANNIHILATIONS/DECAYS

In this section, we examine the signal contribution to the differential photon flux $d\Phi/dE_\gamma$ which arises in DDM scenarios in which the ensemble constituents annihilate/decay to a $\gamma\pi^0$ final state (thereby producing a single "primary" photon), followed by a subsequent decay $\phi^0 \to \gamma\gamma$ (thereby producing two "secondary" photons). We begin with a derivation of the general expression for this signal contribution, followed by a discussion of the distinctive qualitative features in the flux spectrum which arise in these scenarios. Note that the kinematics of the $\phi_n \to \gamma\pi^0 \to \gamma\gamma\gamma$ process is reviewed in the Appendix.

A. Differential photon flux: Quantitative results

In order to derive an expression for the total differential photon flux $d\Phi_n/dE_\gamma$ coming from anniliation and/or decay of the DDM ensemble, we begin by deriving an expression for the photon flux Φ_n coming from each individual ensemble constituent. This is not particularly difficult, as there are only two primary ingredients that enter into such a calculation. The first is the integrated energy density ρ_n (or squared energy density ρ_n^2) of the ϕ_n component along the line of sight:

$$J_n \;\equiv\; \int d\Omega \int_{\rm LOS} d\ell \times \begin{cases} \rho_n^2 & \text{for annihilation} \\ \rho_n & \text{for decay} \;, \end{cases} \tag{3.1}$$

where the differential solid angle $d\Omega$ corresponds to our region of interest on the sky. The second ingredient, by contrast, is the annihilation/decay rate R_n of this component into photons: the decay rate for the ϕ_n component is nothing but Γ_n, while the annihilation rate is given by $\langle\sigma_n v\rangle/4m_n$ where $\langle\sigma_n v\rangle$ is the thermally-averaged cross section for the annihilation process $\phi_n^\dagger\phi_n \to \gamma\pi^0$. Putting the pieces together, the resulting photon flux is then given by $\Phi_n = \mathcal{N}_n(J_n/4\pi)(R_n/m_n)$, where $\mathcal{N}_n \equiv \mathcal{N}_n^{(p)} + \mathcal{N}_n^{(s)} = 3$ is the total number of primary plus secondary photons produced via the annihilation/decay of each ϕ_n.

A priori, it is difficult to determine the individual line-of-sight integrals J_n. However, it is natural to suppose that the energy densities ρ_n of the individual ϕ_n within the galactic halo and within the halos of other galaxies are proportional to their overall cosmological abundances. In other words, we shall assume that $\rho_n/\rho_{\rm tot} = \Omega_n/\Omega_{\rm tot}$, where $\rho_{\rm tot} = \sum_{n=0}^N \rho_n$. Under this assumption, we can then define an overall n-independent "J-factor" which represents the *total* energy density integrated along the line of sight,

$$J \;\equiv\; \int d\Omega \int_{\rm LOS} d\ell \times \begin{cases} \rho_{\rm tot}^2 & \text{for annihilation} \\ \rho_{\rm tot} & \text{for decay} \;, \end{cases} \tag{3.2}$$

whereupon our resulting photon flux Φ_n takes the general form

$$\Phi_n \;=\; \mathcal{N}_n \, \frac{J}{4\pi} \, \frac{\Omega_n}{\Omega_{\rm tot}} \, \frac{\lambda_n}{m_n} \tag{3.3}$$

with

$$\lambda_n \;\equiv\; \begin{cases} \dfrac{\Omega_n}{\Omega_{\rm tot}} \dfrac{\langle\sigma_n v\rangle}{4m_n} & \text{for annihilation} \\ \Gamma_n & \text{for decay} \;. \end{cases} \tag{3.4}$$

For simplicity, we assume that the cross-section for *co*-annihilation processes of the form $\phi_m^\dagger \phi_n \to \gamma\pi^0$ with $m \neq n$ is negligible.

Given the result for the individual flux Φ_n in Eq. (3.3), we can now derive the collective contribution to the *differential* photon flux from the annihilation/decay of the *entire* DDM ensemble. Indeed, this is nothing but the sum over the individual contributions $d\Phi_n/dE_\gamma$ from each of the ϕ_n:

$$\frac{d\Phi}{dE_\gamma} = \sum_{n=0}^{N} \frac{d\Phi_n}{dE_\gamma} = \sum_{n=0}^{N} \frac{J}{4\pi} \frac{\Omega_n}{\Omega_{\rm tot}} \frac{\lambda_n}{m_n} \frac{d\mathcal{N}_n}{dE_\gamma} = \frac{\Phi_0}{3} \sum_{n=0}^{N} \frac{\Omega_n}{\Omega_0} \frac{m_0}{m_n} \frac{\lambda_n}{\lambda_0} \frac{d\mathcal{N}_n}{dE_\gamma} , \quad (3.5)$$

where

$$\frac{d\mathcal{N}_n}{dE_\gamma} = \frac{d\mathcal{N}_n^{(p)}}{dE_\gamma} + \frac{d\mathcal{N}_n^{(s)}}{dE_\gamma} \quad (3.6)$$

represents the differential number of photons per unit E_γ produced via a single annihilation/decay event involving the constituent ϕ_n.

Given the expression in Eq. (3.5), our next step is to understand how Ω_n, λ_n, and m_n depend on n. For an arbitrary collection of dark-sector species, these quantities might not exhibit any regular behavior as functions of n. In a DDM ensemble, however, the abundances, decay widths, and cross-sections of the different components all exhibit specific scaling relations as functions of m_n across the DDM ensemble. Indeed, such scaling relations (whether exact or approximate) tend to emerge naturally as a result of the various theoretical structures underlying these ensembles. Of course, since a gamma-ray telescope is at best only capable of measuring the differential photon flux $d\Phi/dE_\gamma$, we see from Eq. (3.5) that such an instrument is not sensitive to the individual scaling behaviors of these different quantities; rather, it is only sensitive to the scaling behavior of the particular combination $\Phi_n \propto \Omega_n \lambda_n / m_n$. Accordingly, for concreteness, we shall assume that the fluxes Φ_n scale with m_n according to a single power law of the form

$$\Phi_n = \Phi_0 \left(\frac{m_n}{m_0}\right)^\xi = \Phi_0 \left(\frac{\sqrt{s_n}}{\sqrt{s_0}}\right)^\xi \quad (3.7)$$

where the masses/CM energies follow Eqs. (2.6) and (2.7) and where the exponent ξ is taken to be a free parameter. Indeed, this is tantamount to assuming that

$$\frac{\Omega_n}{\Omega_0} \frac{\lambda_n}{\lambda_0} = \left(\frac{m_n}{m_0}\right)^{\xi+1} = \left(\frac{\sqrt{s_n}}{\sqrt{s_0}}\right)^{\xi+1} . \quad (3.8)$$

As such, the exponent ξ reflects the internal theoretical structure of the DDM ensemble under study. Note that this parametrization is applicable to both annihilation and decay, although in general we expect the actual value of ξ for the case of annihilation to differ from that for decay.

This parametrization allows us to recast our expression for the differential photon flux in Eq. (3.5) into the relatively simpler form

$$\frac{d\Phi}{dE_\gamma} = \frac{\Phi_0}{3} \sum_{n=0}^{N} \left(\frac{\sqrt{s_n}}{\sqrt{s_0}}\right)^\xi \frac{d\mathcal{N}_n}{dE_\gamma} . \quad (3.9)$$

Moreover, as discussed in the Introduction, we are primarily interested in the regime for which $\Delta m \ll \Delta E_\gamma$ over the energy range of interest, where ΔE_γ is the energy resolution of the detector. Thus, since we expect $\Delta E_\gamma \lesssim E_\gamma \leq \sqrt{s_N}$, we shall focus on the case in which $\Delta m \ll m_0$ and the sum over n in Eq. (3.9) is well approximated by an integral over the continuous variable $\sqrt{s}$. We then obtain

$$\frac{d\Phi}{dE_\gamma} \approx \frac{\Phi_0}{3\Delta(\sqrt{s})} \int_{\sqrt{s_0}}^{\sqrt{s_N}} d\sqrt{s} \left(\frac{\sqrt{s}}{\sqrt{s_0}}\right)^\xi \frac{d\mathcal{N}}{dE_\gamma} , \quad (3.10)$$

where $\Delta(\sqrt{s})$ is defined in Eq. (2.7) and where $d\mathcal{N}/dE_\gamma$ is the differential number of photons per unit E_γ resulting from an ensemble constituent annihilating or decaying with CM energy $\sqrt{s}$ into a $\gamma\pi^0$ final state, followed by a subsequent decay $\pi^0 \to \gamma\gamma$. Note that the integral in Eq. (3.10) continues to represent a sum over ensemble constituents, with the contribution from any $\sqrt{s}$ representing the contribution from that ensemble constituent which annihilates or decays with CM energy $\sqrt{s}$.

Proceeding further requires knowledge of $d\mathcal{N}/dE_\gamma$. However, this quantity includes contributions from both primary and secondary photons, and these two classes of photons have very different kinematic features. We shall therefore consider each of these classes separately.

As discussed in the Appendix, the primary photons are all monochromatic, occupying a "line" with energy

$$E_{\rm line} = \frac{s - m_{\pi^0}^2}{2\sqrt{s}} . \quad (3.11)$$

There is also only one such photon per constituent decay/annihilation. Thus the primary photon contribution to $d\mathcal{N}/dE_\gamma$ is simply

$$\frac{d\mathcal{N}^{(p)}}{dE_\gamma} = \delta(E_\gamma - E_{\rm line}) , \quad (3.12)$$

whereupon the corresponding contribution to the flux in Eq. (3.10) is given by

$$\frac{d\Phi^{(p)}}{dE_\gamma} \approx \frac{\Phi_0}{3\Delta(\sqrt{s})} \left(\frac{\sqrt{s_*}}{\sqrt{s_0}}\right)^\xi \frac{2s_*}{s_* + m_{\pi^0}^2} \times \Theta(\sqrt{s_*} - \sqrt{s_0})\, \Theta(\sqrt{s_N} - \sqrt{s_*}) \quad (3.13)$$

where $\Theta(x)$ is the Heaviside function and where

$$\sqrt{s_*} \equiv \sqrt{E_\gamma^2 + m_{\pi^0}^2} + E_\gamma . \quad (3.14)$$

Physically, this means that there is only one DM constituent whose decay or annihilation contributes to the primary photon flux at any energy E_γ: this is the constituent whose decay or annihilation occurs with the CM energy $\sqrt{s_*}$ given in Eq. (3.14).

The secondary photons have a different kinematics, however. As discussed in the Appendix, the secondary photons emerging from an ensemble constituent decaying or annihilating with CM energy $\sqrt{s}$ have energies which uniformly populate a "box" whose lower and upper limits are respectively given by

$$E^-_{\rm box} \;=\; \frac{m^2_{\pi^0}}{2\sqrt{s}}\,, \qquad E^+_{\rm box} \;=\; \frac{\sqrt{s}}{2}\,. \tag{3.15}$$

Moreover, there are two secondary photons from each such event. Thus, the normalized contribution from the secondary photons to the differential photon number per unit E_γ is given by

$$\begin{aligned}\frac{d\mathcal{N}^{(s)}}{dE_\gamma} \;&=\; 2\,\frac{\Theta(E_\gamma - E^-_{\rm box})\,\Theta(E^+_{\rm box}-E_\gamma)}{E^+_{\rm box}-E^-_{\rm box}} \\ &=\; \frac{4\sqrt{s}}{s-m^2_{\pi^0}}\,\Theta(E_\gamma - E^-_{\rm box})\,\Theta(E^+_{\rm box}-E_\gamma)\,,\end{aligned} \tag{3.16}$$

whereupon the corresponding secondary photon flux becomes

$$\frac{d\Phi^{(s)}}{dE_\gamma} \;\approx\; \frac{4\Phi_0}{3\Delta(\sqrt{s})}\int_{\sqrt{s_{\rm min}}}^{\sqrt{s_N}} d\sqrt{s}\left(\frac{\sqrt{s}}{\sqrt{s_0}}\right)^{\xi}\frac{\sqrt{s}}{s-m^2_{\pi^0}} \tag{3.17}$$

with

$$\sqrt{s_{\rm min}} \;\equiv\; \min\left[\sqrt{s_N},\,\max\left(\sqrt{s_0},\,2E_\gamma,\,\frac{m^2_{\pi^0}}{2E_\gamma}\right)\right]\,. \tag{3.18}$$

Indeed, for any given value of E_γ, the Heaviside theta-functions in Eq. (3.16) restrict the values of $\sqrt{s}$ which contribute in Eq. (3.17) to those which are compatible not only with our original constraints $\sqrt{s_0}\leq\sqrt{s}\leq\sqrt{s_N}$ but also with the simultaneous constraints $E_\gamma < E^+_{\rm box}$ (which requires $\sqrt{s} > 2E_\gamma$) and $E_\gamma > E^-_{\rm box}$ (which requires $\sqrt{s} > m^2_{\pi^0}/2E_\gamma$). The result in Eq. (3.17) can then be integrated in closed form, yielding

$$\begin{aligned}\frac{d\Phi^{(s)}}{dE_\gamma} \;\approx\; &\frac{2\Phi_0}{3\Delta(\sqrt{s})}\left(\frac{m_{\pi^0}}{\sqrt{s_0}}\right)^{\xi}\times \\ &\left[B_{z_1}(-\xi/2,0)-B_{z_2}(-\xi/2,0)\right]\end{aligned} \tag{3.19}$$

where $B_z(a,b)$ is the incomplete Euler beta-function, with $z_1\equiv m^2_{\pi^0}/s_{\rm min}$ and $z_2\equiv m^2_{\pi^0}/s_N$.

In summary, the overall signal contribution to the differential photon flux in DDM scenarios of this sort is the sum of the two individual contributions from primary and secondary photons given in Eqs. (3.13) and (3.19), respectively.

B. Differential photon flux: Qualitative features

The spectral feature associated with primary photons, which is described by Eq. (3.13), extends between $E_{\rm line}(\sqrt{s_0})$ and $E_{\rm line}(\sqrt{s_N})$. The shape of this feature is in large part dictated by the value of the index ξ. However, since we are focusing on ensembles in which the CM energy for the annihilation/decay of each of the ϕ_n falls within the range $m_{\pi^0} < \sqrt{s_n} < 2m_{\pi^\pm}$, this feature typically appears reasonably flat (unless the value of ξ is extreme) and exhibits a sharp cutoff at $E_\gamma = E_{\rm line}(\sqrt{s_N})$.

By contrast, the spectral feature associated with secondary photons, which is described by Eq. (3.19), has a markedly different shape. As discussed above, the individual contribution to $d\Phi^{(s)}/dE_\gamma$ from each ϕ_n consists of a flat, box-like feature centered at $E_\gamma = m_{\pi^0}/2$ on a logarithmic scale. Thus, the total contribution to the secondary photon flux consists of a "tower" of such boxes centered at this same value of E_γ. Since the width of each box is given by $(s_n - m^2_{\pi^0})/2\sqrt{s_n}$, the narrowest box is associated with the lightest ensemble constituent participating in the relevant annihilation/decay process, and has a width $(s_0 - m^2_{\pi^0})/2\sqrt{s_0}$ if ϕ_0 is indeed that constituent. This implies that in cases in which $\sqrt{s_0}\approx m_{\pi^0}$, a sharp peak or spike appears at the center of the tower [22, 23]. By contrast, in cases in which the difference between $\sqrt{s_0}$ and m_{π^0} is larger — even by a few MeV — the top of the tower appears flat and forms a plateau [17, 22–24]. We thus have

$$\begin{cases}\sqrt{s_0}\approx m_{\pi^0} & \text{spike} \\ \sqrt{s_0} > m_{\pi^0} & \text{plateau}\,.\end{cases} \tag{3.20}$$

Another important consideration is whether and to what extent the spectral features associated with primary and secondary photons in this scenario overlap. Indeed, as we shall see in Sect. V, the degree of overlap between these spectral features determines the fitting procedure which must be used in extracting information about the fundamental parameters governing the DDM ensemble. In particular, in cases in which the two features are well separated, a parametric fit can be performed for each in isolation. By contrast, in cases in which the overlap between the two features is significant, a single fit must be performed on the combined spectrum in order to extract the underlying parameters governing the DDM ensemble. In either case, however, we shall find that it is often possible to measure most of the underlying parameters which characterize the DDM ensemble with reasonable precision.

In order to assess the degree of overlap between the primary and secondary photon spectra for any particular choice of parameters, we compare the maximum possible energy for a primary photon to the minimum possible energy for a secondary photon. The former is given by $E_{\rm line}(\sqrt{s_N})$ while the latter is given by $E^-_{\rm box}(\sqrt{s_N})$. The spectral features associated with the primary and secondary photons will thus overlap only if $E^-_{\rm box}(\sqrt{s_N}) <$

$E_{\rm line}(\sqrt{s_N})$, or equivalently if $\sqrt{s_N} > \sqrt{2}m_{\pi^0}$. We thus have

$$\begin{cases} \sqrt{s_N} < \sqrt{2}m_{\pi^0} & \text{no overlap} \\ \sqrt{s_N} > \sqrt{2}m_{\pi^0} & \text{overlap} \ . \end{cases} \tag{3.21}$$

In order to illustrate the range of different combinations of spectral shapes which can arise in scenarios of this sort, we introduce a set of benchmark parameter choices which exemplify four qualitatively different kinds of spectra. The values of $\sqrt{s_0}$ and $\sqrt{s_N}$ for these benchmarks are given in Table I. For each benchmark we have taken $\Delta\sqrt{s} = 2$ MeV; in this connection we recall that $m_{\pi^0} \approx 135$ MeV, whereupon $\sqrt{2}m_{\pi^0} \approx 191$ MeV. Note that when discussing fluxes, we shall describe our DDM ensembles in terms of the CM energies $\sqrt{s_n}$ characterizing the annihilations/decays of their constituents rather than in terms of their corresponding masses m_n. We do this in recognition of the fact that under the assumption given in Eq. (3.7), the photon fluxes that result from such annihilations or decays depend on these CM energies rather than on the underlying masses. In particular, by describing our ensembles in terms of CM energies rather than masses, we retain maximal generality and need not specify whether our ensemble constituents are annihilating or decaying. Indeed, this information cannot be gleaned from photon fluxes alone, and it is only in mapping our CM energies $\sqrt{s_n}$ back to underlying masses m_n that this information would be required.

The gamma-ray spectra corresponding to the benchmarks in Table I are displayed in Fig. 1, where we have further assumed $\xi = 1$. Note that these plots include the contributions from both primary and secondary photons. Each of the spectra shown in the figure has been normalized so that they all share a common total flux when integrated over all energies E_γ. The black curve in each panel represents the spectrum obtained by superposing the analytic expressions given in Eqs. (3.13) and (3.19). By contrast, the blue histogram represents the results of a Monte-Carlo simulation of the corresponding gamma-ray spectrum as they might be observed by a physical detector. We account for the non-zero energy resolution of the detector by smearing of the initial photon energies obtained in the simulation using a Gaussian smearing function. In particular, we take the probability R_ϵ for the detector to register an energy E_γ, given an actual incoming photon energy E'_γ, to be

$$R_\epsilon(E_\gamma - E'_\gamma) \ = \ \frac{1}{\sqrt{2\pi}\epsilon E'_\gamma} \exp\left[-\frac{(E_\gamma - E'_\gamma)^2}{2(\epsilon E'_\gamma)^2}\right] \ , \tag{3.22}$$

where ϵ is a dimensionless parameter which sets the overall scale of the E'_γ-dependent standard deviation $\sigma_E(E'_\gamma) = \epsilon E'_\gamma$ of the Gaussian. The results in Fig. 1 correspond to a 1% Gaussian smearing — *i.e.*, to the choice $\epsilon = 0.01$.

Benchmark A (top left panel of Fig. 1) is representative of the regime in which $\sqrt{s_0} \approx m_{\pi^0}$ and $\sqrt{s_N} < \sqrt{2}m_{\pi^0}$. In this regime, there is no overlap between the features associated with the contributions from primary and secondary photons, while the feature associated with the secondary photons appears as a spike or peak rather than a plateau. By contrast, Benchmark B (top right panel) is representative of the regime in which $\sqrt{s_0} \approx m_{\pi^0}$ and $\sqrt{s_N} > \sqrt{2}m_{\pi^0}$: the feature associated with the secondary photons likewise appears as a spike, but there is a significant overlap between this feature and the feature associated with the primary photons. Benchmark C (bottom left panel) is representative of the regime in which $\sqrt{s_0}$ is significantly larger than m_{π^0} and $\sqrt{s_N} < \sqrt{2}m_{\pi^0}$: in this regime the features associated with primary and secondary photons do not overlap, but the feature from secondary photons exhibits a plateau rather than a spike. Finally, Benchmark D (bottom right panel) is representative of the regime in which $\sqrt{s_0}$ is significantly larger than m_{π^0} and $\sqrt{s_N} > \sqrt{2}m_{\pi^0}$: in this regime the feature associated with the secondary photons likewise appears as a plateau, but there is a significant overlap between this feature and the feature associated with the primary photons.

IV. DISCOVERY REACH OF FUTURE EXPERIMENTS

We now turn to examine the projected sensitivity of future gamma-ray experiments to DDM ensembles which annihilate/decay primarily to $\gamma\pi^0$, followed by a subsequent decay $\pi^0 \to \gamma\gamma$. Indeed, a variety of proposals have recently been advanced for experiments that would significantly improve the sensitivity to photon signals in the relevant energy range. These include the Advanced Compton Telescope (ACT) [25], the Advanced Pair Telescope (APT) [26], the Gamma-Ray Imaging, Polarimetry and Spectroscopy (GRIPS) detector [27], the Advanced Energetic Pair Telescope (AdEPT) [28], the Pair-Production Gamma-Ray Unit (PANGU) [29], the Compton Spectrometer and Imager (COSI) [30], and the ASTROGAM detector [31].

In our analysis, for concreteness, we consider a hypothetical space-based detector with attributes similar to those of ASTROGAM. In particular, we assume that our detector is sensitive in the energy range 0.3 MeV $\lesssim E_\gamma \lesssim$ 3000 MeV, and we account for the energy resolution of the detector using a Gaussian smearing function of the form given in Eq. (3.22). For simplicity, we take the energy resolution to be 1% (*i.e.*, we take $\epsilon = 0.01$) and we take the effective area to be 500 cm^2 throughout this entire E_γ range. These assumptions represent optimistic projections from the ASTROGAM design specifications, and the actual detector response will be different. In particular, since ASTROGAM will utilize two detector technologies in order to cover different portions of this same E_γ range, its energy resolution and effective area will depend non-trivially on E_γ.

Our goal is to assess the discovery reach of our hy-

Benchmark	$\sqrt{s_0}$ (MeV)	$\sqrt{s_N}$ (MeV)	N	Behavior at $E_\gamma = m_{\pi^0}/2$	Spectral overlap
A	135	181	23	spike	negligible
B	135	231	48	spike	significant
C	164	180	8	plateau	negligible
D	164	230	33	plateau	significant

TABLE I: Four benchmark DDM ensembles — each corresponding to a different choice of the parameters $\sqrt{s_0}$ and $\sqrt{s_N}$ — which illustrate the range of spectral signatures which arise in this scenario. For each of these benchmarks, we have taken $\Delta(\sqrt{s}) = 2$ MeV. The resulting features (spike versus plateau at $E_\gamma = m_{\pi^0}/2$ and the degree of spectral overlap) are governed by the criteria in Eqs. (3.20) and (3.21).

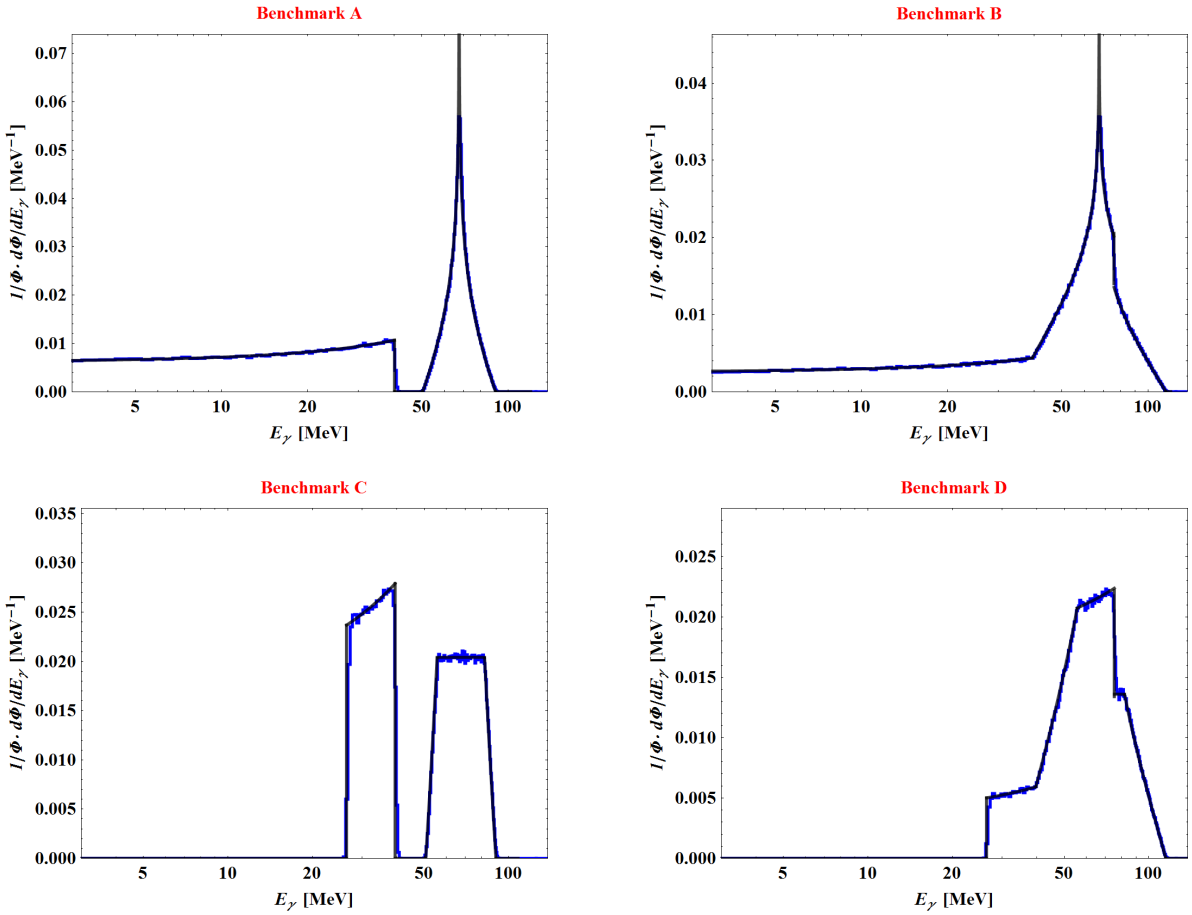

FIG. 1: The differential photon energy spectra associated with the four benchmark parameter choices A through D defined in Table I, where we have taken $\xi = 1$. The black curve in each panel represents the analytic result obtained by superposing the contributions to the photon spectrum given in Eqs. (3.13) and (3.19), while the blue histogram represents the results of a simulated data set smeared according to the Gaussian smearing function in Eq. (3.22).

pothetical detector as a function of the parameters governing our underlying DDM model. We shall assess this discovery reach as follows. First, we define the quantity

$$\frac{\tilde{\Phi}}{J} \;=\; \frac{4\pi}{3J}\sum_n \Phi_n \;=\; \sum_n \frac{\Omega_n}{\Omega_{\rm tot}}\frac{\lambda_n}{m_n} \;\equiv\; \langle \lambda/m \rangle \qquad (4.1)$$

where $\tilde{\Phi} \equiv (4\pi/3)\Phi$ is the normalized total flux that we would expect to see from a given DDM model. In some sense this quantity represents the "particle-physics" contribution to the total flux, with the astrophysical factor J divided out. In order to assess the reach of our hypothetical detector, we therefore seek the critical (minimal) value of $\tilde{\Phi}/J$ for which an excess might become apparent after one year of continuous observation. Or, phrased conversely, we seek to determine the maximum value of $\tilde{\Phi}/J$ for which *no* appreciable signal can be resolved after one year of continuous observation. If this maximum value of $\tilde{\Phi}/J$ is relatively small for a given set of underlying DDM parameters, our telescope is extremely sensitive to the corresponding DDM photon flux and our discovery

reach is enhanced. By contrast, if this maximum value of $\tilde{\Phi}/J$ is relatively large, the corresponding discovery reach of our hypothetical telescope is suppressed.

In our analysis, we shall consider two different regions of interest on the sky which correspond to two of the most promising search strategies for gamma-ray signals of dark-matter annihilation/decay: searches in dwarf spheroidal galaxies and searches in the diffuse galactic gamma-ray spectrum. We do not consider signals from the Galactic Center, as the astrophysical backgrounds in this region are not well understood and systematic uncertainties are therefore expected to be large.

A. Dwarf-spheroidal search

Dwarf spheroidal galaxies provide a particularly auspicious environment in which to search for signals of annihilating/decaying dark matter. Observations of stellar kinematics within these galaxies suggest that they are highly dark-matter dominated [32, 33]. In addition, since the solid angle on the sky subtended by many of these galaxies is small, reasonably reliable empirical estimates of the astrophysical foregrounds and backgrounds can be obtained from measurements of the differential gamma-ray flux in the surrounding region. Moreover, since most known dwarf spheroidals lie at significant distances from the galactic plane of the Milky Way, these astrophysical foregrounds are small.

For concreteness, we focus our analysis on one particular dwarf galaxy, Draco, which subtends a solid angle of approximately 1.6×10^{-3} sr on the sky. For a region of interest defined by this solid angle, an empirical reconstruction of the dark-matter halo profile of this galaxy from stellar-kinematic data [34] yields a J-factor $\log_{10}(J/\mathrm{GeV}^2\mathrm{cm}^{-5}) = 19.05^{+0.22}_{-0.21}$ for annihilation and $\log_{10}(J/\mathrm{GeVcm}^{-2}) = 18.97^{+0.17}_{-0.24}$ for decay. For simplicity, we assume that the main source of foreground/background photons is diffuse emission and assume that contributions from nearby extragalactic sources are negligible. We model the diffuse contribution to the differential gamma-ray flux using a single power law, with a normalization coefficient and scaling index derived from a fit to COMPTEL [35] and EGRET [36] data:

$$\frac{d^2\Phi_b}{dE\,d\Omega} \;=\; 2.74\times 10^{-3}\left(\frac{E}{\mathrm{MeV}}\right)^{-2.0}\mathrm{cm}^{-2}\mathrm{s}^{-1}\mathrm{sr}^{-1}\mathrm{MeV}^{-1}. \tag{4.2}$$

In general, the DDM discovery reach of our hypothetical detector depends on the underlying DDM parameters $\sqrt{s_0}$, $\sqrt{s_N}$, and ξ. (As usual, we are assuming $\delta = 1$ and $\Delta\sqrt{s} = 2$ MeV.) For each choice of parameters, our results in Eqs. (3.13) and (3.19) make a prediction concerning the signal differential fluxes $d\Phi^{(s,p)}/dE_\gamma$ of primary and secondary photons, respectively. In particular, for any given values of $(\sqrt{s_0}, \sqrt{s_N})$, these signal fluxes stretch over only a finite range of energies E_γ. Thus, for any given $(\sqrt{s_0}, \sqrt{s_N})$, we shall restrict our analysis to those energy bins lying within this range.

The choice of $(\sqrt{s_0}, \sqrt{s_N}, \xi)$ determines the overall *shape* of the signal differential flux as a function of photon energy E_γ, while the overall magnitude of this differential flux is determined by the normalization Φ_0. Thus, for any given choice of $(\sqrt{s_0}, \sqrt{s_N}, \xi)$, we then seek to find the critical (minimal) value of Φ_0 for which an excess signal just becomes observable. Equivalently, we seek the largest value of Φ_0 for which *no* signal can be discerned. This largest value of Φ_0 then leads to a corresponding largest value of $\tilde{\Phi}/J$, where the numerical value of J is given above.

In general, there are two different paths we might follow in order to determine this critical value of Φ_0. One possible procedure is to find the critical value of Φ_0 for which an excess *in any single bin* just becomes observable (or equivalently, the largest value of Φ_0 for which no signal can be discerned *in any single bin*). Within each bin, observability would be assessed as follows. In general, the expected number of events within a given bin includes a signal contribution from DDM annihilation/decay within the halo of Draco as well as a background contribution given by Eq. (4.2). We would then seek the maximum value of Φ_0 for which this observed number of events in every bin is consistent with the contribution from background alone within 95% C.L., assuming Poisson statistics.

The above procedure describes a "binned" approach to determining the critical value of $\tilde{\Phi}/J$ which is sensitive to the overall *shape* of the differential flux — *i.e.*, an approach which is based on an analysis of the counts within individual energy bins. However, an alternative path is to simply focus instead on the total integrated flux across all energy bins, and to determine the critical value of $\tilde{\Phi}/J$ for which this integrated flux exceeds the integrated contribution from background alone within 95% C.L., assuming Poisson statistics.

In order to asssess the greatest (maximum) discovery reach, we shall employ whichever method (binned or integrated) yields the smallest value for $\tilde{\Phi}/J$. It turns out that if $\sqrt{s_0} \approx m_{\pi^0}$, the primary photon spectrum extends down to very low photon energies where the diffuse background is quite large. Incorporating these high-background bins into a total (integrated) counting analysis significantly weakens the estimate of the discovery reach. Consequently, for $\sqrt{s_0} \approx m_{\pi^0}$, it turns out that the binned analysis yields a greater discovery reach. For larger values of $\sqrt{s_0}$, by contrast, it turns out that an analysis based on the total integrated flux is superior.

B. Diffuse-background search

The total diffuse gamma-ray background consists of a contribution from unresolved astrophysical sources as well as both a galactic and an extragalactic contribution from dark-matter annihilation/decay. The extragalac-

tic dark-matter contribution is assumed to be isotropic, while the galactic contribution depends (through the J-factor) on the dark-matter halo profile of the Milky Way. However, this latter contribution is not particularly sensitive to the form of the inner halo profile in situations in which the region of interest includes only areas of the sky far from the Galactic Center. Moreover, the diffuse extragalactic contribution to the photon flux from any particular location on the sky is typically subleading in comparison with the diffuse galactic contribution, except for cases in which that location lies near either of the galactic poles (where the latter contribution is presumably at its minimum). Accordingly, we adopt as our region of interest the region in which the galactic latitude b lies within the range $20^\circ < |b| < 60^\circ$. In the following, we calculate the J-factors from their differential forms for an NFW profile, for which numerical evaluations are given in Ref. [37].

Disentangling the dark-matter contribution to the diffuse gamma-ray flux from the astrophysical background requires detailed knowledge of that background. However, the astrophysical contribution to the diffuse gamma-ray flux is not well measured or understood. Given this uncertainty, we evaluate the discovery reach for this diffuse search using two different methods. The first of these involves no assumptions about the astrophysical background and yields a more conservative estimate of the discovery reach, while the second assumes a particular functional form for the background and thereby yields a more optimistic estimate.

In deriving our more conservative estimate of the discovery reach, we compare the gamma-ray flux spectrum observed by our hypothetical detector to the expected signal contribution from dark-matter annihilation/decay alone. More specifically, we compare the number of events observed in each energy bin to the corresponding number of expected events, given a particular choice of DDM model parameters. Under the assumption that the observed number of events in each bin is given by the background spectrum in Eq. (4.2), we derive an upper limit on $\tilde{\Phi}/J$ for which this observed number of events $\mathcal{N}_i^{\rm obs}$ in each bin is consistent with the theoretical expectation $\mathcal{N}_i^{\rm exp}$ to within $2\sigma_i$, where the index i labels the bin and where σ_i denotes the corresponding uncertainty. In particular, σ_i is dominated by systematic uncertainty in the expression for the differential flux in Eq. (4.2), which we take to be 15% of the flux itself.

In deriving our more optimistic estimate of the discovery reach, we follow a procedure which is similar to that followed for the dwarf-spheroidal search. However, rather than neglecting the background contribution to the expected number of events in each bin, in this case we assume that this background contribution is given by Eq. (4.2). Once again, we derive an upper limit on $\tilde{\Phi}/J$ by assuming that the observed number of events in each bin is likewise given by the background spectrum in Eq. (4.2) and requiring consistency between $\mathcal{N}_i^{\rm obs}$ and $\mathcal{N}_i^{\rm exp}$ to within $2\sigma_i$ in each bin.

C. Results

The discovery reaches for both the dwarf-spheroidal search and the diffuse-background search are shown in Fig. 2. In this figure, the bounds on $\tilde{\Phi}/J$ from each search are shown as a function of the parameter $\sqrt{s_N}$ for the four different reference values of $\sqrt{s_0}$ labelled within each panel, with $\Delta\sqrt{s} = 2$ MeV and $\sqrt{s_0} + 10\Delta\sqrt{s} \leq \sqrt{s_N} \leq 2m_{\pi^\pm}$. This lower bound on $\sqrt{s_N}$ ensures that we are including the contributions of at least 10 ensemble constituents ϕ_n in addition to ϕ_0 for each chosen value of $\sqrt{s_0}$, while the upper bound ensures that we do not exceed the threshold $2m_{\pi^\pm}$ for charged-pion pair-production, beyond which additional flux contributions must be included. Results for $\xi = -1, 0, +1$ are shown along the top, middle, and bottom rows of Fig. 2, while the panels within the left and right columns of Fig. 2 show the results for annihilating and decaying dark-matter scenarios respectively. The solid colored bands indicate the results of the dwarf-spheroidal search, with the width of each band reflecting a 1σ uncertainty in the J-factor for the dwarf. By contrast, the dashed and dot-dashed lines correspond to the results of a diffuse-background search using the optimistic and conservative analysis methods outlined in Sect. IV B, respectively.

For the dwarf-spheroidal search, the results shown in Fig. 2 indicate that the discovery reach for our hypothetical telescope tends to be relatively insensitive to $\sqrt{s_N}$ for large $\sqrt{s_0}$, but more sensitive to $\sqrt{s_N}$ for smaller $\sqrt{s_0}$. When scanned over possible values of $\sqrt{s_0}$, however, the discovery reach tends to be relatively insensitive to $\sqrt{s_N}$: cases with large $\sqrt{s_0}$ provide the greatest reach when $\sqrt{s_N}$ is large but cases with smaller $\sqrt{s_0}$ provide the greatest reach when $\sqrt{s_N}$ is smaller.

It is also noteworthy that when $\sqrt{s_0} \approx m_{\pi^0}$, it is the binned analysis which provides the greater discovery reach; the opposite is true when $\sqrt{s_0}$ is larger. However, this can be understood as follows. When $\sqrt{s_0} \approx m_{\pi^0}$, the primary photon spectrum extends down to very low gamma-ray energies where the diffuse background is quite large. Incorporating these high-background bins into an analysis based on total counts then significantly weakens the estimate of the discovery reach. However, this feature does not affect the individually-binned analysis where the effects from such low-energy bins no longer dominate the analysis. Thus, in such cases, the results of the binned analysis are stronger than those of an integrated analysis. Indeed, this is ultimately why the overall discovery reach for small $(\sqrt{s_0}, \sqrt{s_N})$ remains competitive with that for larger values of $(\sqrt{s_0}, \sqrt{s_N})$, as shown in Fig. 2. Indeed, we see from Fig. 2 that this remains true for all of the values of ξ surveyed.

For the diffuse-background search, by contrast, the discovery reach depends more stikingly on both $\sqrt{s_0}$ and $\sqrt{s_N}$. Moreover, the reach is sensitive to the spectral shapes of both the primary and secondary photon contributions to the gamma-ray spectrum. Overall, the secondary photon contribution has a more significant im-

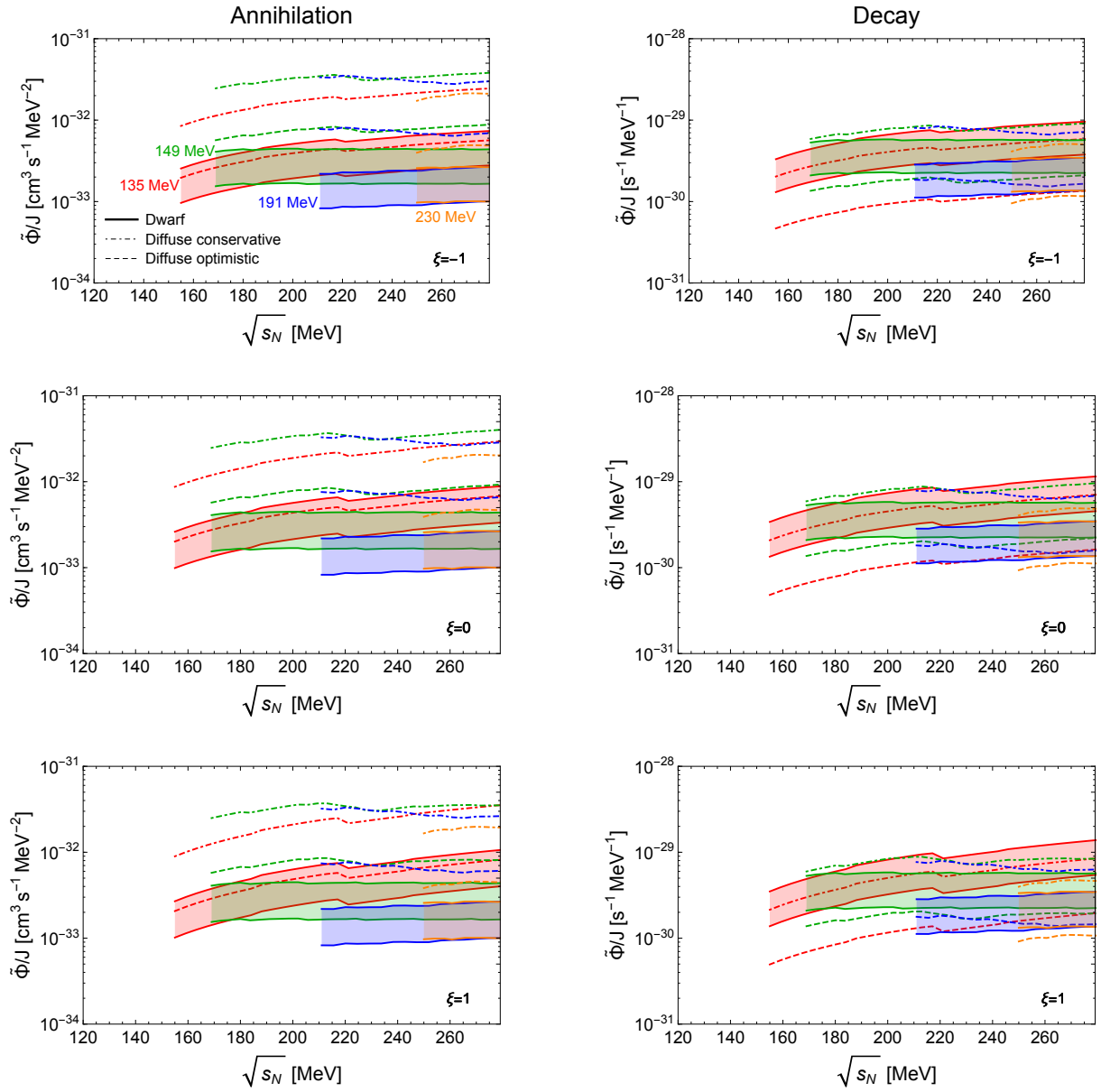

FIG. 2: The projected discovery reach for a representative next-generation MeV-range gamma-ray telescope, plotted as functions of $\sqrt{s_N}$ for different values of $\sqrt{s_0}$ and ξ, with $\Delta(\sqrt{s}) = 2$ MeV. The results are shown as an upper limit on the quantity $\tilde{\Phi}/J$ for which a statistically significant signal is not observed within one year of continuous observation. Panels in the top, middle, and bottom rows correspond to $\xi = -1, 0, +1$, respectively, while those in the left and right columns correspond respectively to annihilating and decaying dark-matter scenarios. Within each panel, four benchmark choices of $\sqrt{s_0}$ are shown: $\sqrt{s_0} = 135$ MeV (red curves), 149 MeV (green curves), $\sqrt{s_0} = 191$ MeV (blue curves), and $\sqrt{s_0} = 230$ MeV (orange curves). In each case we then show results for $\sqrt{s_N}$ within the range $\sqrt{s_0} + 10\Delta\sqrt{s} \leq \sqrt{s_N} \leq 2m_{\pi^\pm}$. The solid bands shown in each panel correspond to the results of the dwarf-spheroidal search, as outlined in Sect. IV A, with the results for $\sqrt{s_0} = 135$ MeV obtained through a binned approach and the others obtained through an approach based on the total integrated flux. The width of each band reflects a 1σ uncertainty in the J-factor for the dwarf. The dashed and dot-dashed lines correspond to the results of a diffuse-background search using the optimistic and conservative analysis methods outlined in Sect. IV B, respectively.

pact on the discovery potential. The reason is that in the regime in which $\sqrt{s_N}$ is reasonably small and $\sqrt{s_0} \approx m_{\pi^0}$, the secondary photon spectrum is sharply peaked around $E_\gamma = m_{\pi^0}/2$. As a result, the potential for observing an excess in the corresponding energy bin has a profound positive effect on the overall discovery reach. Indeed, it is evident from Fig. 2 that the reach is greatest in the regime in which $\sqrt{s_N}$ is relatively small and $\sqrt{s_0} \approx m_{\pi^0}$. As $\sqrt{s_0}$ increases away from m_{π^0} and the peak becomes a plateau, the potential for observing an excess in this bin decreases. Increasing $\sqrt{s_N}$ for fixed $\sqrt{s_0}$ has the effect of broadening the secondary photon spectrum. On

the one hand, this broadening reduces the significance of the peak at $E_\gamma = m_{\pi^0}/2$; on the other hand, it also extends the upper edge of the secondary photon spectrum to higher E_γ, where the astrophysical background is smaller and a signal is more readily observable. As a result of the interplay between these two effects, the discovery reach initially falls with increasing $\sqrt{s_N}$ because the energy bin corresponding to the peak provides the best prospects for observing an excess in signal events. However, as $\sqrt{s_N}$ increases further and the higher-energy bins become the most relevant for observing an excess, the discovery potential stabilizes.

While the role played by the primary photon spectrum in determining the discovery reach for the diffuse-background search is less pronounced than that played by the secondary photon spectrum, the primary photon spectrum still has a demonstrable effect on the discovery reach. In particular, as $\sqrt{s_0}$ increases, the primary photon spectrum is shifted to higher values of E_γ where astrophysical backgrounds are small. For sufficiently large $\sqrt{s_0}$, this effect more than compensates for the corresponding broadening of the secondary photon spectrum and yields an overall increase in the discovery reach.

Comparing the cases of dark-matter annihilation and decay, we see that the dwarf search has an order-of-magnitude greater discovery reach than the diffuse search for annihilation, while both searches have comparable discovery reaches for decay. Since the J-factor in Eq. (3.2) depends on ρ^2 for annihilation, we expect the dense environment of the dwarf to be a more advantageous system in which to search for annihilating dark matter than the diffuse background. For decay, however, the J-factor involves only a single power of ρ, and thus the dwarf search does not possess the same upper hand as it has for annihilation.

V. EXTRACTION OF DARK-SECTOR PARAMETERS

As discussed in the Introduction, our primary motivation for studying DDM ensembles whose constituents annihilate/decay primarily into a $\gamma\pi^0$ final state, followed by the subsequent decay $\pi^0 \to \gamma\gamma$, is that the shapes of the spectral features associated with primary and secondary photons are correlated. A comparison between the information extracted from these two features can therefore provide a powerful consistency check on the DDM interpretation of such a gamma-ray excess. However, we are not merely interested in the prospects for *observing* a signal of a DDM ensemble with this annihilation/decay phenomenology, as in Sect. IV; we are also interested in determining the degree to which we might then *extract* the values of the underlying parameters which characterize the DDM ensemble. This is the subject to which we now turn.

Towards this end, we shall focus on the four benchmarks outlined in Table I and illustrated in Fig. 1 with $\xi = 1$. For each benchmark, we shall investigate the prospects for extracting the corresponding underlying DDM model parameters $(\sqrt{s_0}, \sqrt{s_N}, \xi)$ by generating and then analyzing corresponding sets of simulated detector data. We begin our discussion by outlining how these data sets are generated and analyzed. We then discuss the extent to which our underlying DDM parameters can be meaningfully extracted in each case. Specifically, using the simulated detector data for each benchmark, we shall focus on two critical but somewhat distinct questions:

- To what extent can we extract *evidence* of a correlation between primary and secondary photon flux spectra?
- To what extent does the *assumption* of such a correlation *enhance* our ability to extract the corresponding underlying DDM model parameters?

Note that a positive outcome to the first question implicitly strengthens our interpretation of a measured photon flux as resulting from annihilating/decaying dark matter (as opposed to, say, other astrophysical sources). By contrast, once we are assured that such a photon flux has a dark-matter origin, such a correlation between the primary and secondary photon fluxes is *automatic*. It is then the second question above which becomes critical for extracting the underlying physics of the dark sector.

A. Generating and analyzing simulated data sets

In order to generate our simulated data sets, we begin by determining the total expected number N_B of background events observed by our hypothetical detector within our region of interest during one year of continuous observation. This number N_B is therefore evaluated across the entire energy range 0.3 MeV $< E_\gamma <$ 3000 MeV to which the detector is sensitive, yielding the result $N_B \approx 2.32 \times 10^5$. Likewise, we determine a number N_S of signal events by assuming the minimum necessary in order to claim a 5σ discovery based on a simple counting analysis in which the statistical significance is estimated using $N_S/\sqrt{N_B}$. This yields $N_S \approx 5\sqrt{N_B} \approx 2.41 \times 10^3$. In principle, one might argue that the values of N_B and N_S should depend on the energy range over which the particular benchmark can be expected to provide data and thereby be sensitive to background. However, since there are relatively few background events in the high-energy regime, it turns out that the above values of N_B and N_S, as calculated for our hypothetical detector as a whole, are not significantly different from those that would correspond to Benchmark B, which has the largest energy range. In the following, we will take the above values of N_B and N_S to be fixed across all benchmarks. This allows us to make a meaningful comparison across benchmarks by considering our fixed quantity to be the number of signal

events itself (rather than, say, a corresponding statistical significance). This procedure for calculating signals and backgrounds across the entire energy range to which our hypothetical detector is sensitive also reflects what one would actually do upon faced with an experimental signal — namely, analyze this signal over the entire energy range available, without any foreknowledge or assumptions regarding the particular underlying spectral features involved.

Given the above values of N_B and N_S, the generation of our simulated data set for each benchmark proceeds as follows. The signal contribution associated with each ensemble constituent is determined by partitioning the N_S signal events among the ϕ_n in proportion to the contribution Φ_n that each makes toward the total photon flux Φ. Photon energies for background events are generated randomly from the relevant probability distribution function over the entire range mentioned above. Photon energies for the set of signal events associated with a given ϕ_n are also generated randomly, with one third of the events assigned the primary photon energy $E_{\rm line}$ given in Eq. (3.11) and the other two thirds distributed according to a normalized probability distribution function derived from Eq. (3.16). Finally, the raw E_γ values for both signal and background events are smeared according to Eq. (3.22) with $\epsilon = 0.01$ in order to account for the energy resolution of the detector.

The net result of this procedure is a set of four simulated energy spectra that might emerge from the decays/annihilations of our four DDM "benchmark" ensembles. Our analysis of these data sets then proceeds as follows. First, recognizing that these data sets represent the total "observed" differential photon fluxes, we begin by disentangling our "signal" contribution from astrophysical backgrounds. For this reason, we focus exclusively on dwarf-spheroidal searches, as the corresponding backgrounds can be estimated directly from measurements. For concreteness, we consider the same region of interest which characterized the dwarf-spheroidal search in Sect. IV A and adopt the same set of parameters for our hypothetical detector. To isolate the signal contribution, we employ a minimal background-subtraction procedure in which an expected number of background events $\mathcal{N}_i^{\rm BG}$ in each energy bin is derived using the background model in Eq. (4.2) and is subtacted from the corresponding total number of observed events $\mathcal{N}_i^{\rm Data}$. Again, we emphasize that we can follow this procedure because experimentalists will actually be able to measure the background, unlike the situation in the case of a diffuse search. The resulting number of events

$$\mathcal{N}_i^{\rm Sig} \equiv \mathcal{N}_i^{\rm Data} - \mathcal{N}_i^{\rm BG} \tag{5.1}$$

is thus our "signal" contribution, to be interpreted as coming from the decays/annihilations of the constituents of the DDM ensemble.

Given this signal contribution, we determine the corresponding values of the underlying DDM shape parameters $(\sqrt{s_0}, \sqrt{s_N}, \xi)$ by fitting the template functions in Eqs. (3.13) and (3.19) to this residual spectrum. However, the specific fit we perform will depend on which of the fundamental questions itemized above we are attempting to answer.

To address the first question, we perform *independent* fits of the primary and secondary flux spectra, extracting independent best-fit values $(\sqrt{s_{0,p}}, \sqrt{s_{N,p}}, \xi_p)$ for the primary flux spectra and $(\sqrt{s_{0,s}}, \sqrt{s_{N,s}}, \xi_s)$ for the secondary flux spectra. Comparing these sets of parameters with each other thus provides a test of our purported correlations between these two spectra. Likewise, comparing each independent set of parameters against our corresponding original benchmark values provides a measure of our ability to extract our underlying DDM parameters *without* assuming a correlation between the two spectra. By contrast, to address the second question, we perform a constrained fit of *both* spectra simultaneously with only a single set of free parameters $(\sqrt{s_0}, \sqrt{s_N}, \xi)$. Comparing the results thus obtained with those previously obtained with independent fits for each spectrum then provides a measure of the extent to which the existence of a correlation between the two spectra enhances our ability to extract the underlying DDM model parameters.

In practice, it is important to recognize that there is actually another variable beyond the shape variables $(\sqrt{s_0}, \sqrt{s_N}, \xi)$ which must also be fit when extracting our underlying DDM parameters: this is the overall normalization factor Φ_0. In fact, strictly speaking, the overall normalization factor for both the primary photon spectrum in Eq. (3.13) and the secondary photon spectrum in Eq. (3.19) is not Φ_0 alone, but rather the parameter combination

$$\Psi \equiv \Xi\,(\sqrt{s_0})^{-\xi}\,, \tag{5.2}$$

where

$$\Xi \equiv \frac{\Phi_0}{\Delta(\sqrt{s})}\,. \tag{5.3}$$

We shall therefore fit the aggregate quantity Ψ directly, and only subsequently extract a value for Ξ using the results of our overall fits for $\sqrt{s_0}$ and ξ. Unfortunately, without *a priori* knowledge of $\Delta(\sqrt{s})$, we see that the parameter combination Ξ cannot be disentangled further and thus represents the irreducible limit of our ability to extract the underlying DDM flux normalization using these methods.

As briefly discussed in Sect. III B, the procedure that we shall use in performing these parametric fits to the signal spectrum depends on the degree of overlap between the spectral features associated with primary and secondary photons. In the regime in which $\sqrt{s_N} < \sqrt{2} m_{\pi^0}$, these two features are well separated and a fit can be performed for each feature independently. Indeed, this will be our procedure for Benchmarks A and C. By contrast, in the regime in which $\sqrt{s_N} > \sqrt{2} m_{\pi^0}$, the overlap is significant and a single fit must be performed for both features simultaneously. This will be our procedure for Benchmarks B and D.

Thus, summarizing, the specific types of fits we shall perform depend not only on which of the questions itemized above we are seeking to address, but also on which benchmark we are studying. To address the first question for Benchmark A, we shall perform two independent four-parameter fits, extracting independent values $(\sqrt{s_{0,p}}, \sqrt{s_{N,p}}, \xi_p, \Psi_p)$ and $(\sqrt{s_{0,s}}, \sqrt{s_{N,s}}, \xi_s, \Psi_s)$ using our data sets for the primary and secondary spectra respectively. We also follow an identical procedure in order to address the first question for Benchmark C. Indeed, it is only because these two spectra are non-overlapping for Benchmarks A and C that we allow each fit to have its own independent normalization in these cases. By contrast, in order to address the first question for Benchmark B or Benchmark D, we perform a single seven-parameter fit to the parameters $(\sqrt{s_{0,p}}, \sqrt{s_{N,p}}, \xi_p, \sqrt{s_{0,s}}, \sqrt{s_{N,s}}, \xi_s, \Psi)$. Indeed, in these cases, the overlapping nature of the primary and secondary photon spectra requires that we impose a common normalization Ψ during the fitting process. Of course, the results of this fit then yield independent values for $\Xi_p = \Psi(\sqrt{s_{0,p}})^{\xi_p}$ and $\Xi_s = \Psi(\sqrt{s_{0,s}})^{\xi_s}$. Finally, in order to address the second question for each benchmark, we compare the above results with those obtained through a single four-parameter fit to the underlying DDM parameters $(\sqrt{s_0}, \sqrt{s_N}, \xi, \Psi)$.

Note that this analysis applies equally well for either annihilation or decay, as the only difference between these two cases lies not in the extracted values of the $\sqrt{s_n}$ parameters but rather in the subsequent mapping between these parameters and the original DDM mass variables m_n, as already discussed in Sects. II and III [especially Eq. (2.3)] and at the end of the Appendix.

B. Results

The results of our analysis are as follows. For each of the benchmarks listed in Table I, our corresponding simulated data set is shown in Fig. 3 (black dots with error bars). Specifically, these dots represent the residual populations of events $\mathcal{N}_i^{\rm Sig}$ in the relevant energy bins, with error bars corresponding to statistical uncertainties. Also superimposed on these data sets are the results of parametric fits to the spectral features associated with primary and secondary photons (solid red lines). Recall that in these plots, the spectral features associated with the primary and secondary flux spectra are fit independently. As discussed above, these are the fits which are designed to address the first question itemized above.

The results for Benchmark A are shown in the upper left panel of Fig. 3. For Benchmark A, our value of N_S translates into the result

$$\Xi \;=\; 5.4 \times 10^{-9}\ {\rm cm}^{-2}\,{\rm s}^{-1}\,{\rm MeV}^{-1}\ , \qquad (5.4)$$

which we take as our input value for this benchmark. We perform our fit to the primary photon spectrum for Benchmark A within the energy range 20 MeV $\leq E_\gamma \leq$ 45 MeV — indeed, the region $E_\gamma <$ 20 MeV is background-dominated, leaving the corresponding bin counts less reliable, given our signal statistics. We find that the best-fit values for ξ_p and $\sqrt{s_{N,p}}$ are those indicated in the upper left panel of Fig. 3. It is immediately evident that these extracted values are consistent with the corresponding input values to within 1σ. Note that no meaningful information can be extracted for $\sqrt{s_{0,p}}$, as large uncertainties in the event counts in bins with $E_\gamma \lesssim$ 20 MeV completely obscure all meaningful information about the low-energy cutoff in the primary photon spectrum. Thus, a best-fit value for Ξ is not available from the primary photon spectrum, as this would require the value for $\sqrt{s_{0,p}}$.

By contrast, a fit to the secondary photon spectrum for Benchmark A provides far more reliable information about the properties of the underlying DDM ensemble. Performing such a fit within the energy range 50 MeV $\leq E_\gamma \leq$ 90 MeV where the residual bin counts are greater than ~ 10, we find the results shown in the upper left panel of Fig. 3. Once again, each of these extracted values is in good agreement with the corresponding input value to within 1σ. Since we are able to meaningfully extract $\sqrt{s_0}$ for the secondary photon spectrum, we are also able to report the best-fit value for Ξ in this case. We find that the best-fit value for the normalization parameter is

$$\Psi_s \;=\; 4.8^{+275.9}_{-4.8} \times 10^{-11}\ {\rm cm}^{-2}\,{\rm s}^{-1}\,{\rm MeV}^{-1-\xi}\ , \qquad (5.5)$$

from which we obtain the value of Ξ for the secondary photon spectrum:

$$\Xi_s \;=\; 3.0^{+169.0}_{-12.3} \times 10^{-9}\ {\rm cm}^{-2}\,{\rm s}^{-1}\,{\rm MeV}^{-1}\ . \qquad (5.6)$$

Although this extracted value is consistent with the input value in Eq. (5.4) to within 1σ, the corresponding uncertainty is too large to infer any useful information.

Thus, for Benchmark A, we conclude that it is difficult to obtain meaningful information concerning the normalization parameter Ξ from either the primary or secondary photon spectrum. By contrast, we see that reasonable estimates of the parameters which govern the *shapes* of the primary and secondary photon spectra can indeed potentially be obtained from future gamma-ray detectors. Moreover, the fact that the values of DDM parameters such as $\sqrt{s_N}$ and ξ extracted from the primary photon spectrum match those extracted from the secondary photon spectrum implies that we can indeed perform a successful test of the underlying correlations between these two spectra, and indicates that our primary and secondary spectra together contain consistent information regarding the underlying DDM model.

We now turn to Benchmark B, for which results are shown in the upper right panel of Fig. 3. For this benchmark, the signal events are produced within the energy range 135 MeV $< \sqrt{s} <$ 231 MeV, requiring us to take

$$\Xi \;=\; 2.3 \times 10^{-9}\ {\rm cm}^{-2}\,{\rm s}^{-1}\,{\rm MeV}^{-1} \qquad (5.7)$$

as an input value. Since the primary and secondary photon spectra overlap significantly for this benchmark, we

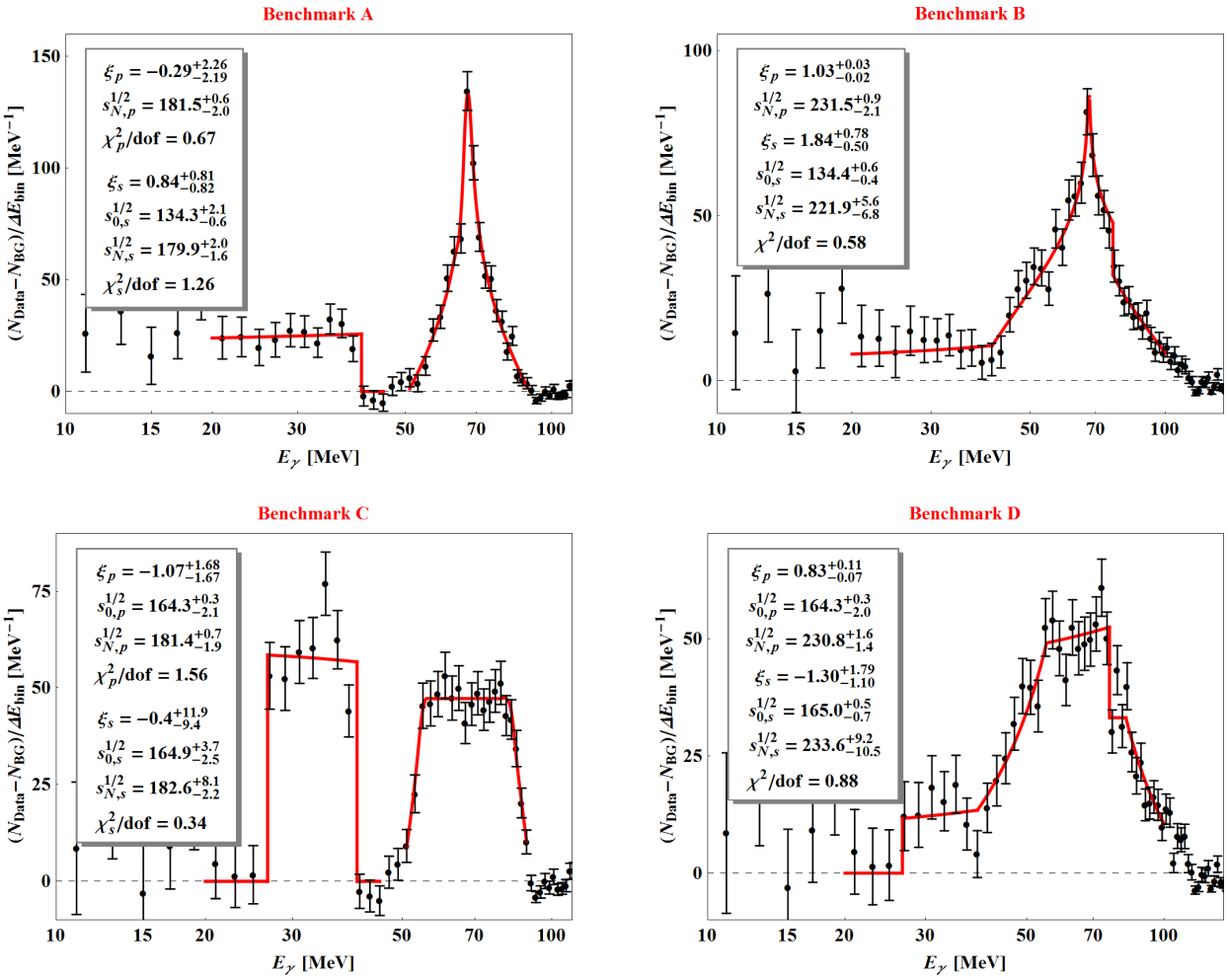

FIG. 3: Sample photon-energy spectra (black dots with corresponding statistical error bars) for Benchmarks A (upper left panel), B (upper right panel), C (lower left panel), and D (lower right panel) after background subtraction, along with the corresponding best fits for the primary and secondary photon spectra (solid red curves). For each benchmark, the numbers of background and signal events are taken to be $N_B = 2.32 \times 10^5$ and $N_S = 2.41 \times 10^3$, as discussed in the text. Note that we plot the quotient $(N_{\rm Data} - N_{\rm BG})/\Delta E_{\rm bin}$ on the vertical axis (where the numerator tabulates the signal counts within each bin and the denominator indicates the corresponding bin size), as this quotient is invariant under changes in the specific choice of bin size when the bin size is sufficiently small. The corresponding error bars, by contrast, depend on bin size, and we have chosen $\Delta E_{\rm bin} = 2$ MeV for the curves in these plots. The best-fit parameters are also indicated within each panel, along with the corresponding goodness-of-fit χ^2 per degree of freedom, while the upper and lower uncertainties quoted for each best-fit parameter indicate the limits of the corresponding range within which χ^2 varies by less than one unit. Note that the fits performed here are *unconstrained*, in the sense that the primary and secondary photon spectra are fit independently. These fits thus provide a test of the extent to which the correlations between these two spectra can be discerned from data.

perform a combined fit to both features in the manner discussed above, taking our fitting range to be 20 MeV $\leq E_\gamma \leq$ 100 MeV. We then obtain the best-fit values for the shape parameters given in Fig. 3. Once again, we observe that the parameters ξ and $\sqrt{s_N}$ extracted for both spectra agree reasonably well with each other, thus providing a rough test of their correlation. Moreover, each of the extracted shape parameters listed in the upper right panel of Fig. 3 is consistent with the corresponding input value to within $(1-2)\sigma$.

Thus, for Benchmark B, we conclude that our fitting procedure yields reasonable estimates for the shape parameters which characterize the photon spectrum associated with our DDM ensemble. The best-fit value of Ψ, by contrast, comes with large uncertainties. Indeed, we shall find that this is a characteristic of all of the benchmarks we shall be examining. We shall therefore refrain from quoting further best-fit values for Ψ and Ξ in what follows. However, we stress that in all cases this is strictly only an artifact of the parametrization and does not represent a corresponding uncertainty in actual signal flux or in the number of signal events (the uncertainty for which is indeed small).

Note that Benchmark B provides a better handle for

measuring the DDM scaling parameter ξ accurately, especially when compared to ξ_p in Benchmark A. This is ultimately because more signal events in Benchmark B are populated in the higher-energy regime where the background contribution is relatively small. Therefore, even after background subtraction, the residual spectrum for Benchmark B better preserves the original shape information than it does for Benchmark A.

For the remaining two benchmarks, even the primary photon spectrum has a reasonable sensitivity to $\sqrt{s_0}$ because it starts from $E_\gamma > 20$ MeV where uncertainties in the event counts in bins are fairly decent. Our results for Benchmark C are shown in the lower left panel of Fig. 3. The signal events are generated with 164 MeV $< \sqrt{s} <$ 180 MeV, from which we find that

$$\Xi \;=\; 1.6 \times 10^{-8}\ \mathrm{cm}^{-2}\,\mathrm{s}^{-1}\,\mathrm{MeV}^{-1}\ . \qquad (5.8)$$

As with Benchmark A, the two photon spectra are well separated, and thus two individual fits are possible. We adopt the same energy ranges as for Benchmark A, namely 20 MeV $\leq E_\gamma \leq$ 45 MeV and 50 MeV $\leq E_\gamma \leq$ 90 MeV, respectively, for our fits to the primary and secondary photon spectra, and obtain the best-fit results for the shape parameters as shown in the figure. The parameters for the primary and secondary photon spectra are generally consistent with each other, thus indicating the possibility of testing correlations between them, and they are also in a good agreement with the corresponding input values to within $(1-2)\sigma$. It turns out that the overall shape of the secondary photon spectrum does not change much for this benchmark, even with substantial variations of the scaling parameter.

Results for Benchmark D are shown in the lower right panel of Fig. 3. The signal events are generated with 164 MeV $< \sqrt{s} <$ 230 MeV, from which we find

$$\Xi \;=\; 3.7 \times 10^{-9}\ \mathrm{cm}^{-2}\,\mathrm{s}^{-1}\,\mathrm{MeV}^{-1}\ . \qquad (5.9)$$

We then perform a single combined fit to both photon spectra, again adopting the same fitting range 20 MeV $\leq E_\gamma \leq$ 100 MeV as for Benchmark B. The best-fit values for all shape parameters are listed in Fig. 3. We can easily see that the parameters measured from both spectral features are consistent with each other, as expected. The extracted values also all agree with the corresponding input values to within $(1-2)\sigma$.

In general, scanning the results in Fig. 3 for all four benchmarks simultaneously, we see that our best-fit results for $\sqrt{s_0}$ and $\sqrt{s_N}$ are generally quite accurate. Unfortunately, we also observe that these fits generally do a poor job of extracting the true underlying values of the DDM scaling parameter ξ. While certain benchmarks (such as Benchmark B) lead to relatively accurate best-fit values for ξ, particularly for the primary photon spectrum, these predictions become significantly worse for those benchmarks (such as Benchmarks A and C) in which the spectral features associated with the primary and secondary photons are relatively well-separated in energy, with minimal overlap. The case of Benchmark C is particularly poor, with *negative* central values of ξ extracted from both the primary and secondary spectra! Indeed, the negative central value for ξ_p is reflected in the negative slope of the red best-fit line along the primary plateau in the lower left panel of Fig. 3.

All of the fits performed thus far treat our primary and secondary photon spectra independently. As discussed above, they are therefore suitable for addressing the first bulleted question at the beginning of this section concerning the extent to which correlations between the two photon fluxes might be discernible in realistic data samples. However, in order to address the second of our bulleted questions, we need to assume the existence of such correlations and perform constrained fits to both spectra simultaneously. Indeed, it is only by performing such constrained fits and comparing the results thus obtained with those of the unconstrained fits we have already perfomed that we can determine the extent to which these correlations enhance our ability to extract the underlying DDM parameters from data.

The results of such constrained fits are shown in Fig. 4. Upon comparison with the corresponding results in Fig. 3, we immediately see that while our extracted best-fit values of $\sqrt{s_0}$ and $\sqrt{s_N}$ continue to be as accurate as they were before, our extracted best-fit values for the DDM scaling parameter ξ are significantly improved. Indeed, in all cases the true value $\xi = 1$ is within the errors quoted. The case of Benchmark C is particularly noteworthy. Where previously our unconstrained fits had yielded negative values for both ξ_p and ξ_s, the simple act of changing to a constrained fit has pushed the corresponding best-fit result to a central value $\xi = 1.01$, which is remarkably close to the true value! In general, we see that it is Benchmarks A and C — *i.e.*, benchmarks in which our two spectral features are well separated in energy — for which the switch from an unconstrained fit to constrained fit produces the greatest improvement. It is thus these benchmarks for which the assumption of a correlation between the primary and secondary photon spectra is of greatest value. Indeed, as evident from Fig. 4, the assumption of a correlation between the primary and secondary flux spectra leads to a signficant improvement in our ability to extract the underlying DDM parameters regardless of the particular benchmark under study.

Of course, our comparison between the fits in Fig. 3 and those in Fig. 4 amounts to analyzing the results of only a single pseudo-experiment. In principle, one could rerun this experiment with many different random data sets, and repeat this analysis in each case. However, we shall refrain from this exercise because the main points that we have aimed to demonstrate are already evident. Indeed, the results illustrated in Figs. 3 and 4 prove to be both typical and robust.

We conclude, then, that it will indeed be possible to extract evidence of a correlation between primary and secondary photon spectra at future gamma-ray facilities.

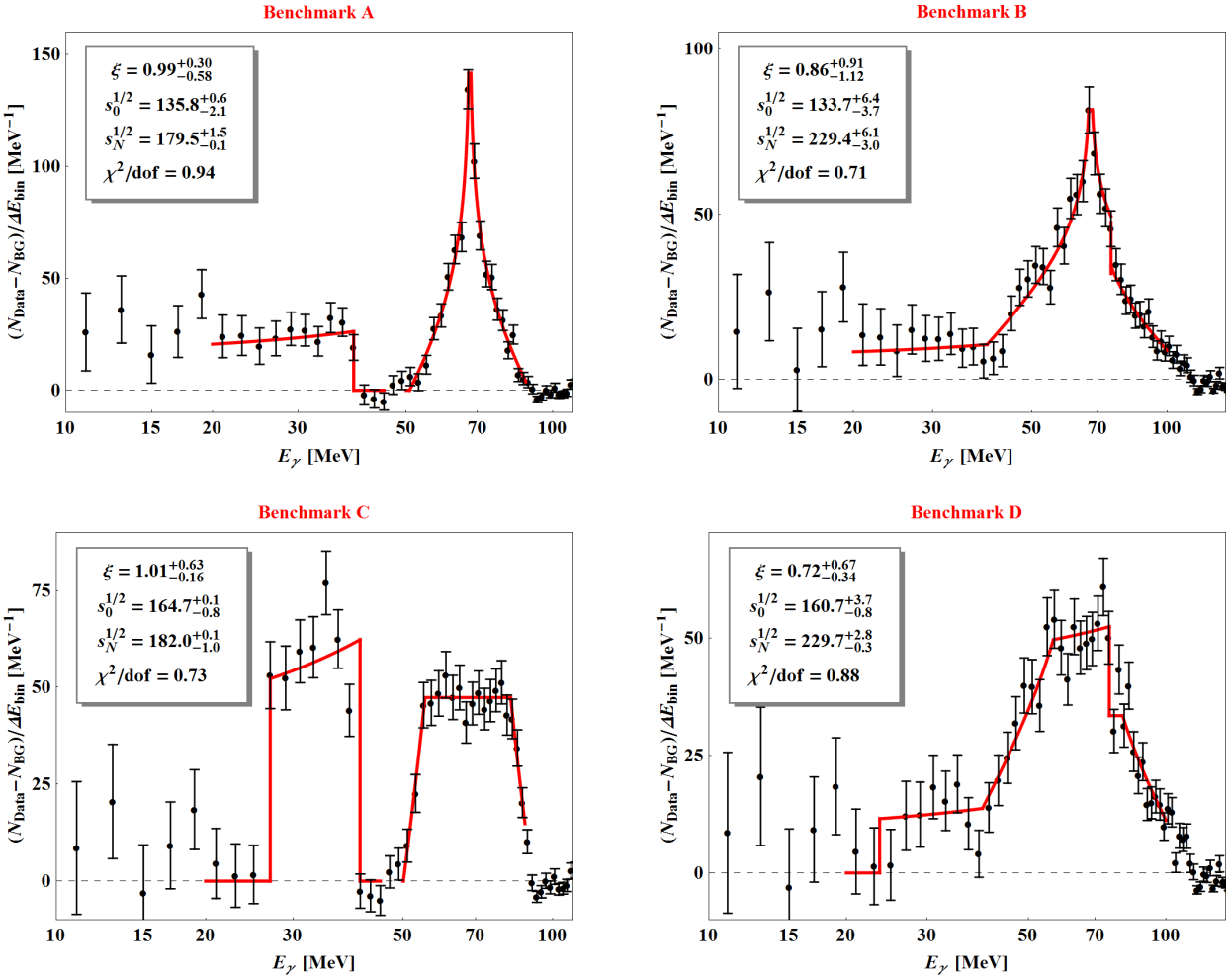

FIG. 4: Same as Fig. 3, except that we now perform *constrained* fits in which the primary and secondary photon spectra are assumed to be correlated. A comparison with the results of Fig. 3 demonstrates that the assumption of such correlations can significantly enhance our ability to accurately extract the underlying DDM parameters governing the dark sector.

Moreover, we see that the assumption of such a correlation will indeed significantly sharpen our ability to extract the corresponding underlying dark-sector parameters. Thus, through this correlation, we see that our ability to indirectly probe the physics of the dark sector through emitted gamma-rays can be greatly enhanced.

VI. CONCLUSIONS AND OUTLOOK

In this paper, we have identified an unambiguous indirect-detection signature of Dynamical Dark Matter which arises in cases in which the constituents of the DDM ensemble annihilate or decay primarily into a final state involving a primary photon and a neutral pion, the latter subsequently decaying into a pair of secondary photons. When the mass gap between DDM constituents is sufficiently small that particle detectors are unable to resolve the contributions of individual constituents in the photon energy spectra, this signature involves a pair of characteristic *continuum* features in the gamma-ray spectrum in the $\mathcal{O}(1-100)$ MeV range — one feature associated with the primary photons, and the other feature associated with the secondary photons. Since the spectral shapes of these two features are correlated, a comparison between the information extracted from the two continuum features provides a powerful consistency check that they indeed have a common origin in terms of an underlying DDM ensemble. We have examined the prospects for observing a signal of this sort at the next generation of MeV-range gamma-ray telescopes and investigated the extent to which the parameters which govern the DDM ensemble can be extracted from spectral data once such a signal is unambiguously identified. As we have seen, it should be possible not only to extract evidence of this correlation in future photon spectral data, but also to exploit this correlation in order to significantly enhance our ability to extract these underlying DDM parameters.

A few comments are in order. First, in order to maintain maximum generality, we emphasize that we have

estimated both the discovery reach and the potential for measuring the DDM model parameters at the next generation of gamma-ray detectors by defining a simplified, hypothetical detector whose attributes have been chosen not to be identical to those of any particular such instrument, but rather to be representative of this class of experiments in general. However, for a realistic detector, the corresponding analysis would typically involve additional subtleties and complications. For example, the energy resolution for such a detector is typically not described by a Gaussian smearing function with a constant value of ϵ. Moreover, the effective area for a realistic detector is typically not independent of photon energy throughout the range of E_γ to which the instrument is sensitive.

In addition to these experimental simplifications, there are also a number of theoretical approximations which we have employed in our analysis. For example, we have taken the branching fraction for the annihilation/decay of all ensemble constituents to the $\gamma\pi^0$ final state to be effectively unity. However, there are situations in which this is not necessarily true for the lightest ensemble constituents. The reason is that a fundamental interaction between the ϕ_n and SM quarks of the sort which leads to dark-matter annihilation/decay to $\gamma\pi^0$ also generically leads to annihilation/decay to e^+e^- and/or $\mu^+\mu^-$, via loop-level processes involving a virtual photon. The branching fraction into such leptonic final states is typically negligible for most of the ϕ_n. However, it can become significant for processes in which the CM energy is only slightly above the kinematic threshold $\sqrt{s}_n \approx m_{\pi^0}$ for $\gamma\pi^0$ production. As a result, the sharpness of the peak in the secondary photon spectrum at $E_\gamma \approx m_{\pi^0}/2$ depends both on $\sqrt{s_0}$ and on the energy resolution of the detector. Incorporating these considerations into a more detailed analysis would inevitably lead to a modification of our quantitative results in DDM scenarios of this sort.

On a related note, we remark that our focus in this paper has been on the case in which that the dominant signal contribution to the photon flux arises from ensemble constituents whose CM energy for annihilation/decay lies within the range $m_{\pi^0} \leq \sqrt{s} \leq 2m_{\pi^\pm}$. However, it is also useful to consider how our results would be affected if non-trivial contributions to the photon flux were also to arise from constituents with $\sqrt{s}$ outside this range, and thus from photoproduction processes with different kinematics. For example, it is important to examine whether such contributions might obscure the spectral features which we have discussed in this paper.

We begin by considering the contribution from constituents with $\sqrt{s}$ slightly above the $2m_{\pi^\pm}$ threshold, for which the dominant C-odd final state will be $\pi^+\pi^-$. The principal contribution from the photon flux in this case arises from final-state radiation. Photons produced in this way tend to be quite soft, and as a result, any contamination of our signal spectrum from such photons would primarily affect the region where E_γ is low and statistical power is already poor. By contrast, for the $\gamma\pi^0$ final state which has been the focus of our paper, at least one of the two salient spectral features always appears at a relatively high energy. For constituents with even larger $\sqrt{s}$, for which final states involving three or more pions are accessible, the shape of the resulting photon spectrum becomes highly model-dependent. However, one generally expects these spectra to be relatively smooth and featureless over the range of E_γ relevant for our analysis.

Now let us turn to the contribution from constituents with $\sqrt{s} < m_{\pi^0}$. For $\sqrt{s}$ in this regime, the dominant contribution to the photon flux arises from the final state 3γ, and from final-state radiation produced in conjunction with the final state e^+e^-. The former contribution is associated with processes involving an off-shell π^0, while the latter is associated with processes involving an off-shell photon attached to a quark loop. Photons produced in conjunction with the e^+e^- final state will once again be quite soft and consequently have little impact on our results. By contrast, the contribution from the 3γ final state could potentially distort the shape of the secondary-photon spectrum at energies slightly below its peak.

In this paper, we have applied our analysis to a DDM ensemble in which the photon flux scales with the center-of-mass energy as a power law. Examples of explicit DDM models in which such behavior is exhibited include those in Refs. [1, 2]. Indeed, as noted above Eq. (3.7), scaling relations of this form tend to emerge naturally for a variety of theoretical structures underlying these ensembles. However, there do exist DDM constructions in which such scaling relations are given not by simple power laws but by other functional forms [19, 20]. These situations can nevertheless be addressed in a manner similar to that which we have employed in this paper. In general, the photon flux is determined by the scaling of the abundance and annihilation/decay rate as in Eq. (3.3). Thus, for any other DDM construction, one can similarly determine the primary and secondary photon fluxes. In fact, it is not even necessary for the dark sector to constitute a DDM ensemble at all. Even if the dark sector consists of multiple particles whose lifetimes and abundances are not determined by any unified organizing principle, those lifetimes and annihilation/decay rates completely determine the primary and secondary differential photon fluxes.

The lynchpin of this paper has been the correlation between the spectral shapes of the primary and secondary photon fluxes. Fortunately, this correlation is robust and survives even if the dark sector lacks a unified organizing principle. To see this most directly, we recall that each dark-sector constituent of a given mass makes only a single monochromatic contribution to the primary photon flux. Thus, the relation between the primary flux and the underlying dark-sector component masses is easily invertible: if the primary flux is known, then one can easily determine the spectrum of particles and annihilation/decay rates which generated that primary spectrum. This in turn then provides a prediction for the secondary

photon flux.

Using the primary photon flux to predict the secondary photon flux is a strategy that is likely to be most useful in the case where $\sqrt{s_N} < \sqrt{2}m_{\pi^0}$, for which the primary and secondary photon features can be cleanly separated. Indeed, after subtracting the estimated background from the data in the region of the primary feature, the residuals constitute a measurement of the primary photon flux, up to statistical fluctuations and the smearing due to the energy resolution. One could then use this primary photon flux to generate a prediction for the secondary flux, and test the goodness of fit for this prediction to the actual data in the region of the secondary feature. However, since the determination of the primary photon flux is distorted by the statistical fluctuations and the effects of a finite energy resolution, the implementation of this strategy is likely to be non-trivial. This would therefore be an interesting direction for future study.

In cases for which $\sqrt{s_N} > \sqrt{2}m_{\pi^0}$, by contrast, the primary and secondary photon features are expected to overlap significantly. As a result, it may be more problematic to cleanly separate them. Despite this fact, we have already seen that these two features remain correlated and in the case of a DDM ensemble we have seen that this correlation can significantly enhance our ability to extract the underlying DDM parameters — even when these features overlap significantly. In general, however, performing an *a priori* separation of the primary and secondary photon features will undoubtedly be a more complicated task in the cases where these features overlap. One useful tool in this regard may be to exploit the so-called "log-symmetry" of the secondary photon flux — *i.e.*, the invariance of this flux under the energy-inversion symmetry $E \to m_{\pi^0}^2/4E$, as discussed in the Appendix. Any contributions to the total flux which violate this symmetry are necessarily those from the primary photons.

Finally, in closing, we remark that correlations between continuum features which arise in the gamma-ray spectra of annihilating/decaying DDM ensembles arise not only for the $\gamma\pi^0$ final state which has been the focus of this paper, but for other final states as well. For example, in DDM scenarios in which each of the ensemble constituents can annihilate into both $\gamma\gamma$ and γZ, similar correlations between the shapes of the two resulting spectral features can likewise be exploited in order to corroborate the DDM origin of the excess and to extract information about the parameters governing the underlying ensemble. Thus, such correlations could likewise be used in order to extract information about this alternative class of DDM ensembles.

Acknowledgments

We would like to thank Kaustubh Agashe and Graciela Gelmini for useful discussions. We would also like to acknowledge the hospitality of the Center for Theoretical Underground Physics and Related Areas (CETUP*), where this work was initiated during the 2015 Summer Program; DK, JK, JCP, and BT would also like to thank CETUP* for partial support during this program. KB and JK are supported in part by the National Science Foundation under CAREER Grant PHY-1250573, while KRD is supported in part by the Department of Energy under Grant DE-FG02-13ER41976 and by the National Science Foundation through its employee IR/D program. DK is supported in part by the U.S. Department of Energy under Grant DE-SC0010296, and JCP is supported in part by the Basic Science Research Program through the National Research Foundation of Korea funded by the Ministry of Education (NRF-2013R1A1A2061561). BT is supported in part by an internal research award from Reed College. The opinions and conclusions expressed herein are those of the authors, and do not represent any funding agencies.

Appendix A: The Line and the Box: Decay Kinematics for the Process $\phi_n \to \gamma\pi^0 \to \gamma\gamma\gamma$

This appendix is dedicated to a quick review of the decay kinematics [13, 22, 23] associated with the primary decay process $\phi_n \to \gamma\pi^0$, followed by the secondary decay process $\pi^0 \to \gamma\gamma$. Our goal is to calculate the spectrum of energies of the photons produced through these processes, as measured in the lab (detector) frame, assuming that our initial ensemble constituent ϕ_n with mass m_n decays from rest in this frame.

Understanding the primary decay process $\phi_n \to \gamma\pi^0$ is relatively straightforward. With ϕ_n taken to be at rest at the time of its decay, conservation of energy and momentum immediately lead to the two constraint equations

$$\begin{aligned} m_n &= E_\gamma^{(1)} + m_{\pi^0}\gamma_\pi \\ E_\gamma^{(1)} &= m_{\pi^0}\gamma_\pi\beta_\pi = m_{\pi^0}\gamma_\pi\sqrt{1-1/\gamma_\pi^2} \end{aligned} \tag{A1}$$

where $E_\gamma^{(1)}$ is the energy of the primary photon and where (γ_π, β_π) denote the boost factor and corresponding velocity of the emitted on-shell pion. Solving these equations, we find that the energy $E_\gamma^{(1)}$ of the primary photon is given by

$$E_\gamma^{(1)} = \frac{m_n^2 - m_{\pi^0}^2}{2m_n} \tag{A2}$$

while (γ_π, β_π) are given by

$$\gamma_\pi = \frac{m_n^2 + m_{\pi^0}^2}{2m_n m_{\pi^0}}\,, \qquad \beta_\pi = \frac{m_n^2 - m_{\pi^0}^2}{m_n^2 + m_{\pi^0}^2}\,. \tag{A3}$$

Thus the lab-frame energy of the emitted pion is given by

$$E_\pi = m_{\pi^0}\gamma_\pi = \frac{m_n^2 + m_{\pi^0}^2}{2m_n}\,. \tag{A4}$$

The second step is to determine the energies of the secondary photons. In the rest frame of the emitted pion, these energies are nothing but $m_{\pi^0}/2$. However our goal is to determine these energies as measured in the lab frame. To do this, we need to account for the boost of the emitted pion. Let us assume that one of the secondary photons is emitted at an angle θ, as measured in the rest frame of the pion, relative to the boost direction of the pion. We then find that lab-frame energy of this secondary photon is given by

$$\begin{aligned} E_\gamma^{(2)} &= \frac{m_{\pi^0}}{2}\gamma_\pi\left(1+\beta_\pi\cos\theta\right) \\ &= \frac{1}{4m_n}\left[m_n^2+m_{\pi^0}^2+(m_n^2-m_{\pi^0}^2)\cos\theta\right]. \end{aligned} \tag{A5}$$

The lab-frame energy of the other secondary photon is given by the same expression, but with $\theta \to \theta+\pi$, or $\cos\theta \to -\cos\theta$.

The interpretation of these results is clear. When many such ϕ_n decays occur, the primary photons always have the energy $E_\gamma^{(1)}$ given in Eq. (A2). They are thus mono-chromatic, forming a spectral line (*i.e.*, occupying a discrete point in energy space). By contrast, the secondary photons can populate any of the energies given in Eq. (A5), depending on the angle θ. Since the probability distribution for photon emission is isotropic in the rest frame of the pion, all values of $\cos\theta$ are sampled with equal probability. As a result, with enough decays, the secondary photons fill out a spectral "box" in energy space. This spectral box stretches over the range $[m_{\pi^0}^2/2m_n, m_n/2]$ and is centered at $E_\gamma = (m_n^2+m_{\pi^0}^2)/4m_n$ with width $\Delta E_\gamma = (m_n^2-m_{\pi^0}^2)/2m_n$.

Interestingly, it turns out that the energy of the line always happens to be equal to the width of the box! For $m_n < \sqrt{2}m_{\pi^0}$, the line is to the left of the box, while for $m_n > \sqrt{2}m_{\pi^0}$, the line is *inside* the box. As $m_n \to \infty$, the line approaches the right edge of the box but never passes beyond it.

It is worth noting that there is only one value for the energy which *always* finds itself within this box, regardless of the width of the box (*i.e.*, regardless of the boost of the pion or the value of m_n): this is $E_\gamma = m_{\pi^0}/2$, corresponding to the energy of the secondary photons in the pion rest frame [22, 23]. This is indeed nothing but the location of the line to which the box collapses as $m_n \to m_{\pi^0}$. This is also the *geometric mean* of the energies encompassed within the box. Indeed, since the box is otherwise flat as a function of the energy, the energy spectrum of the secondary photons is actually "log-symmetric" [*i.e.*, invariant under the mapping $E \to m_{\pi^0}^2/4E$, or equivalently $y \to -y$ where $y \equiv \log(2E/m_{\pi^0})$]. While these assertions are somewhat trivial for the spectrum corresponding to the secondary photons from the decays of a single field ϕ_n, the fact that these features are independent of m_n guarantees that they will be preserved even for the accumulated spectra of secondary photons emitted via the decays of *multiple* ϕ_n with different masses m_n. Indeed, this holds true *regardless* of the particular structure of the underlying DDM ensemble to which the ϕ_n belong. Note that these assertions form the centerpiece of Ref. [23], where they were exploited in a collider-based context.

Our analysis above has focused on the kinematics of the decay process $\phi_n \to \gamma\pi^0 \to \gamma\gamma\gamma$. However, in this paper we are also interested in the corresponding annihilation process $\phi_n^\dagger\phi_n \to \gamma\pi^0 \to \gamma\gamma\gamma$. Fortunately, given the analysis above, it is not difficult to extract the corresponding results for the case of annihilation rather than decay: under the assumption that the ϕ_n are extremely non-relativistic with respect to the lab frame, the only required change in the above analysis is the global replacement $m_n \to 2m_n$. Thus, given the definition of $\sqrt{s_n}$ in Eq. (2.3), we see that the replacement $m_n \to \sqrt{s_n}$ everywhere in the above analysis will generalize our results to apply to ϕ_n annihilations as well as decays. This is the procedure followed in the main text.

[1] K. R. Dienes and B. Thomas, Phys. Rev. D **85**, 083523 (2012) [arXiv:1106.4546 [hep-ph]].

[2] K. R. Dienes and B. Thomas, Phys. Rev. D **85**, 083524 (2012) [arXiv:1107.0721 [hep-ph]].

[3] K. R. Dienes, J. Kumar and B. Thomas, Phys. Rev. D **86**, 055016 (2012) [arXiv:1208.0336 [hep-ph]].

[4] K. R. Dienes, J. Kumar and B. Thomas, Phys. Rev. D **88**, no. 10, 103509 (2013) [arXiv:1306.2959 [hep-ph]].

[5] K. R. Dienes, S. Su and B. Thomas, Phys. Rev. D **86**, 054008 (2012) [arXiv:1204.4183 [hep-ph]].

[6] K. R. Dienes, S. Su and B. Thomas, Phys. Rev. D **91**, no. 5, 054002 (2015) [arXiv:1407.2606 [hep-ph]].

[7] K. Agashe, D. Kim, M. Toharia and D. G. E. Walker, Phys. Rev. D **82**, 015007 (2010) doi:10.1103/PhysRevD.82.015007 [arXiv:1003.0899 [hep-ph]].

[8] K. Agashe, D. Kim, D. G. E. Walker and L. Zhu, Phys. Rev. D **84**, 055020 (2011) doi:10.1103/PhysRevD.84.055020 [arXiv:1012.4460 [hep-ph]].

[9] W. S. Cho, D. Kim, K. T. Matchev and M. Park, Phys. Rev. Lett. **112**, no. 21, 211801 (2014) doi:10.1103/PhysRevLett.112.211801 [arXiv:1206.1546 [hep-ph]].

[10] K. Agashe, R. Franceschini and D. Kim, JHEP **1411**, 059 (2014) doi:10.1007/JHEP11(2014)059 [arXiv:1309.4776 [hep-ph]].

[11] O. Adriani *et al.* [PAMELA Collaboration], Nature **458**, 607 (2009) doi:10.1038/nature07942 [arXiv:0810.4995 [astro-ph]]; Phys. Rev. Lett. **111**, 081102 (2013) doi:10.1103/PhysRevLett.111.081102 [arXiv:1308.0133 [astro-ph.HE]].

[12] M. Aguilar *et al.* [AMS Collaboration], Phys. Rev. Lett. **110**, 141102 (2013).

doi:10.1103/PhysRevLett.110.141102;
L. Accardo *et al.* [AMS Collaboration], Phys. Rev. Lett. **113**, 121101 (2014). doi:10.1103/PhysRevLett.113.121101

[13] K. K. Boddy and J. Kumar, Phys. Rev. D **92**, no. 2, 023533 (2015) doi:10.1103/PhysRevD.92.023533 [arXiv:1504.04024 [astro-ph.CO]].

[14] A. Ibarra, S. Lopez Gehler and M. Pato, JCAP **1207**, 043 (2012) doi:10.1088/1475-7516/2012/07/043 [arXiv:1205.0007 [hep-ph]].

[15] C. Garcia-Cely and J. Heeck, arXiv:1605.08049 [hep-ph].

[16] D. Kim and J. C. Park, Phys. Dark Univ. **11**, 74 (2016) doi:10.1016/j.dark.2016.01.001 [arXiv:1507.07922 [hep-ph]].

[17] D. Kim and J. C. Park, Phys. Lett. B **750**, 552 (2015) doi:10.1016/j.physletb.2015.09.070 [arXiv:1508.06640 [hep-ph]].

[18] K. R. Dienes and B. Thomas, Phys. Rev. D **86**, 055013 (2012) [arXiv:1203.1923 [hep-ph]].

[19] K. R. Dienes, J. Fennick, J. Kumar and B. Thomas, Phys. Rev. D **93**, no. 8, 083506 (2016) [arXiv:1601.05094 [hep-ph]].

[20] K. R. Dienes, F. Huang, S. Su and B. Thomas, Phys. Rev. D **95** (2017) no.4, 043526 [arXiv:1610.04112 [hep-ph]].

[21] D. Chialva, P. S. B. Dev and A. Mazumdar, Phys. Rev. D **87**, no. 6, 063522 (2013) doi:10.1103/PhysRevD.87.063522 [arXiv:1211.0250 [hep-ph]].

[22] F. W. Stecker, "Cosmic gamma rays," *NASA Special Publication* **249** (1971).

[23] K. Agashe, R. Franceschini and D. Kim, Phys. Rev. D **88**, no. 5, 057701 (2013) [arXiv:1209.0772 [hep-ph]].

[24] C. Y. Chen, H. Davoudiasl and D. Kim, Phys. Rev. D **89**, no. 9, 096007 (2014) [arXiv:1403.3399 [hep-ph]].

[25] S. E. Boggs *et al.* [Larger ACT Collaboration], New Astron. Rev. **50**, 604 (2006), astro-ph/0608532.

[26] J. H. Buckley and APT Collaboration, "The Advanced Pair Telescope (APT) Mission Concept," in *AAS/High Energy Astrophysics Division* #10, vol. 10, p. #37.04. Mar., 2008.

[27] J. Greiner *et al.*, Exper. Astron. **34**, 551 (2012) doi:10.1007/s10686-011-9255-0 [arXiv:1105.1265 [astro-ph.HE]].

[28] S. D. Hunter *et al.*, Astropart. Phys. **59**, 18 (2014) doi:10.1016/j.astropartphys.2014.04.002 [arXiv:1311.2059 [astro-ph.IM]].

[29] X. Wu, M. Su, A. Bravar, J. Chang, Y. Fan, M. Pohl and R. Walter, Proc. SPIE Int. Soc. Opt. Eng. **9144**, 91440F (2014) doi:10.1117/12.2057251 [arXiv:1407.0710 [astro-ph.IM]].

[30] C. A. Kierans, S. E. Boggs, A. Lowell, J. Tomsick, A. Zoglauer, M. Amman, J.-L. Chiu, H.-K. Chang, C.-H. Lin, P. Jean, P. von Ballmoos, C.-Y. Yang, J.-R. Shang, C.-H. Tseng, Y. Chou, and Y.-H. Chang, "Calibration of the Compton Spectrometer and Imager in preparation for the 2014 balloon campaign," in *Space Telescopes and Instrumentation 2014: Ultraviolet to Gamma Ray*, vol. 9144 *of Society of Photo-Optical Instrumentation Engineers (SPIE) Conference Series*, p. 91443M. Montreal, Quebec, Canada, July, 2014.

[31] ASTROGAM Collaboration, `http://astrogam.iaps.inaf.it/index.html`.

[32] M. Mateo, Ann. Rev. Astron. Astrophys. **36**, 435 (1998) doi:10.1146/annurev.astro.36.1.435 [astro-ph/9810070].

[33] A. W. McConnachie, Astron. J. **144**, 4 (2012) doi:10.1088/0004-6256/144/1/4 [arXiv:1204.1562 [astro-ph.CO]].

[34] A. Geringer-Sameth, S. M. Koushiappas, and M. Walker, Astrophys. J. **801**, 74 (2015) [arXiv:1408.0002 [astro-ph.CO]].

[35] G. Weidenspointner, "The Origin of the Cosmic Gamma-Ray Background in the COMPTEL Energy Range," PhD Thesis, Technical University of Munich (1999).

[36] A. W. Strong, I. V. Moskalenko, and O. Reimer, Astrophys. J. **613**, 956 (2004) [arXiv:astro-ph/0405441].

[37] M. Cirelli *et al.*, JCAP **1103**, 051 (2011) Erratum: [JCAP **1210**, E01 (2012)] doi:10.1088/1475-7516/2012/10/E01, 10.1088/1475-7516/2011/03/051 [arXiv:1012.4515 [hep-ph]].